

Dynamics of tidal spiral arms: Machine learning-assisted identification of equations and application to the Milky Way

Marcel Bernet^{1,2,3}, Pau Ramos⁴, Teresa Antoja^{1,2,3}, Adrian Price-Whelan⁵,
Steven L. Brunton^{6,7}, Tetsuro Asano^{1,2,3}, and Alexandra Girón-Soto^{1,2,3}

¹ Departament de Física Quàntica i Astrofísica (FQA), Universitat de Barcelona (UB), c. Martí i Franquès, 1, 08028 Barcelona, Spain
e-mail: mbernet@fqa.ub.edu

² Institut de Ciències del Cosmos (ICCUB), Universitat de Barcelona (UB), c. Martí i Franquès, 1, 08028 Barcelona, Spain

³ Institut d'Estudis Espacials de Catalunya (IEEC), Edifici RDIT, Campus UPC, 08860 Castelldefels (Barcelona), Spain

⁴ National Astronomical Observatory of Japan, Mitaka-shi, Tokyo 181-8588, Japan

⁵ Center for Computational Astrophysics, Flatiron Institute, 162 Fifth Ave, New York, NY 10010, USA

⁶ Department of Mechanical Engineering, University of Washington, Seattle, Washington 98195, USA

⁷ AI Institute in Dynamic Systems, University of Washington, Seattle, WA 98195, USA

Received YYY; accepted XXX

ABSTRACT

Context. Understanding the spiral arms of the Milky Way (MW) remains a key open question in galactic dynamics. Tidal perturbations, such as the recent passage of the Sagittarius dwarf galaxy (Sgr), could play a significant role in exciting them.

Aims. We aim to analytically characterize the dynamics of tidally induced spiral arms, including their phase-space signatures.

Methods. We ran idealized test-particle simulations resembling impulsive satellite impacts, and used the Sparse Identification of Non-linear Dynamics (SINDy) method to infer their governing Partial Differential Equations (PDEs). We validated the method with analytical derivations and a realistic N -body simulation of a MW-Sgr encounter analogue.

Results. For small perturbations, a linear system of equations was recovered with SINDy, consistent with predictions from linearised collisionless dynamics. In this case, two distinct waves wrapping at pattern speeds $\Omega \pm \kappa/m$ emerge. For large impacts, we empirically discovered a non-linear system of equations, representing a novel formulation for the dynamics of tidally induced spiral arms. For both cases, these equations describe wave properties like amplitude and pattern speed, and their shape and temporal evolution in different phase-space projections. In the realistic simulations, we recovered the same equation. However, the fit is sub-optimal, pointing to missing terms in our analysis, such as velocity dispersion and self-gravity. We fit the *Gaia* $L_Z - \langle V_R \rangle$ waves with the linear model, providing a reasonable fit and plausible parameters for the Sgr passage. However, the predicted amplitude ratio of the two waves is inconsistent with observations, supporting a more complex origin for this feature (e.g. multiple passages, bar, spiral arms).

Conclusions. We merge data-driven discovery with theory to create simple, accurate models of tidal spiral arms that match simulations and provide a simple tool to fit *Gaia* and external galaxy data. This methodology could be extended to model complex phenomena like self-gravity and dynamical friction.

Key words. Galaxy: disc – Galaxy: kinematics and dynamics – Galaxy: structure – Galaxy: evolution – Methods: data analysis

1. Introduction

Understanding the dynamics of the spiral arms of the Milky Way (MW) remains a major challenge in galactic astronomy (Dobbs & Baba 2014; Sellwood & Masters 2022). Theoretical models of the dynamics of the spiral arms range from density wave theories (Lin & Shu 1964; Kalnajs 1973), to transient and recurrent, swing-amplified instabilities (Goldreich & Lynden-Bell 1965; Julian & Toomre 1966), and self-excited spiral modes (Sellwood & Carlberg 1984), with varying consequences on the spiral pattern speed, pitch angle, and bar-spiral coupling (Lynden-Bell & Kalnajs 1972; Sanders & Huntley 1976; Sellwood & Masters 2022). In the MW, although spiral arm segments can be traced by young stars and gas (Georgelin & Georgelin 1976; Drimmel & Spergel 2001; Reid et al. 2009), their number, longevity, and origin are still debated.

The *Gaia* mission (Gaia Collaboration et al. 2016) has revealed complex kinematic substructures across various phase space projections, $R - V_\phi$ plane (e.g. Antoja et al. 2018; Kawata et al. 2018; Fragkoudi et al. 2019; Ramos et al. 2018; Bernet

et al. 2024), wave-like patterns in $R - V_R$ and $L_Z - V_R$ (e.g. Friske & Schönrich 2019; Eilers et al. 2020; Antoja et al. 2022; Hunt et al. 2024), thin arches in $V_R - V_\phi$ (e.g. Gaia Collaboration et al. 2018; Bernet et al. 2022, 2024), and a vertical phase spiral in $Z - V_Z$ (e.g. Antoja et al. 2018; Laporte et al. 2019; Bland-Hawthorn & Tepper-García 2021; Hunt et al. 2021; Antoja et al. 2023; Darragh-Ford et al. 2023). Interpreting the origin and evolution of these global disequilibrium features requires theoretical modelling that accounts for the effects of the bar, spiral arms, and perturbations with external galaxies.

In Antoja et al. (2022, hereafter A22), motivated by the evidence of ongoing vertical phase mixing in the disc (Antoja et al. 2018) probably due to the interaction with the Sagittarius (Sgr) dwarf galaxy (Ibata et al. 1994), we developed a framework to interpret some of the planar features observed in the MW disc in terms of tidally induced spiral arms. By combining analytical models with test particle simulations and an N -body model of the Sgr-MW interaction (Laporte et al. 2018), we showed how a tidal impact produces spiral arms that phase-wrap over time

and manifest as coherent ridges in $R - V_\phi$ and waves in $L_z - V_R$. However, in A22 we were only able to derive analytically the spiral arm loci as a function of time. This limitation is the result of a hard-to-overcome problem: some dynamical processes readily captured in simulations can prove remarkably challenging to model within an analytical framework.

While a deep foundation in theoretical and analytical models has historically shaped our understanding of galactic dynamics (e.g. Binney & Tremaine 2008), the explosion of high-precision data and modern simulations is transforming the field. This presents an interesting opportunity: the development of new data-driven approaches. Instead of relying on pre-defined models, we can now use the data itself to empirically explore, characterize, and potentially uncover the underlying dynamical principles governing galactic evolution, opening powerful new avenues for dynamical discovery. Inferring physical laws from data is a long-standing practice in astronomy. Centuries ago, Kepler employed what we might now consider a form of symbolic regression to derive his empirical laws of planetary motion (Kepler 1609). More recently, within galactic astronomy, and with significantly different methodology, studies by Tenachi et al. (2023, 2024) have introduced a general deep learning framework for extracting analytical governing laws from simulated and/or observed data, which they successfully applied to derive an analytic galaxy potential directly from simulated stellar orbits approximating stellar streams.

Beyond these examples in astronomy, significant advancements have been made in data-driven methods for discovering the governing equations of complex dynamical systems across various scientific domains. A pioneering approach is SINDy (Sparse Identification of Nonlinear Dynamics), introduced by Brunton et al. (2016), which uses sparse regression to identify the active terms in the governing ordinary differential equations (ODEs) of a dynamical system directly from time-series data. This idea was subsequently extended to partial differential equations (PDEs) by Rudy et al. (2017) and Schaeffer (2017), utilizing spatial-temporal data. Techniques such as the integral or weak formulation (Schaeffer & McCalla 2017; Reinbold et al. 2020) have further refined these methods, improving robustness to noisy data and enabling the handling of high-order derivatives, which are key challenges in empirical law discovery for complex systems. These advances have enabled the data-driven discovery (or rediscovery) of governing PDEs in various physical domains, including geophysical fluids (Zanna & Bolton 2020), plasma physics (Alves & Fiuza 2022), active matter (Supekar et al. 2023), and turbulence closure modelling (Beetham & Capecelatro 2020; Schmelzer et al. 2020; Zanna & Bolton 2020; Beetham et al. 2021). A comprehensive review of these methods is provided by North et al. (2023). Other related techniques for discovering dynamical systems, particularly for ordinary differential equations, include symbolic regression through genetic programming (Bongard & Lipson 2007; Schmidt & Lipson 2009; Cranmer 2023).

In this work, we use a data-driven dynamical discovery approach to understand tidally induced spiral arm dynamics. We build idealised test-particle simulations (Sect. 2) and combine them with machine learning (SINDy) to empirically infer governing equations (Sect. 3). This approach reveals two families of PDEs that govern spiral wave evolution. For small perturbations, we recovered a linear system of equations, consistent with predictions derived from established linearised collisionless theory. For large perturbations with specific profiles, SINDy empirically identified a non-linear system of equations. Notably, this PDE itself constitutes a novel mathematical formulation for

the dynamics of tidally induced spiral arms. Guided by these empirical findings, we analytically derive these same equations from first principles (Sect. 4), recovering closed expressions for their coefficients and obtaining explicit solutions that allow us to describe wave properties like amplitude and pattern speed, and their shape and temporal evolution in different phase-space projections. This framework is validated against realistic N-body simulations (Sect. 5). Finally, we use these analytical solutions to test whether our simple models can reproduce the characteristics of the $L_z - \langle V_R \rangle$ wave seen in the *Gaia* data (Sect. 6). Our work demonstrates how data-driven methods can lead to the discovery of simple governing equations that can be solved analytically and provide interpretable, predictive models for key kinematic features observed in the MW and other galaxies perturbed by internal or external forces.

2. Test particle simulations for tidal impacts

In this section we describe the 2D test particle simulations we use in this work. We run them with Agama (Vasiliev 2019). We used the classical `MWPotential2014` (Bovy 2015), consisting of a Miyamoto & Nagai (1975) disk, a NFW (Navarro et al. 1996) halo and a Dehnen (1993) bulge. The type of dynamical features that we study would be present in any reasonable axisymmetric potential (logarithmic, Plummer, etc), and, thus, our results do not depend on this choice. We initialize all test particles on perfectly circular orbits, with zero velocity dispersion. Thus, each particle satisfies:

$$V_R = 0 \text{ km s}^{-1} \quad V_\phi = V_c \quad (1)$$

where V_c is the circular velocity curve of the assumed model. We sampled 10^6 particles using a uniform distribution in R to increase the signal in the outer disc.

Once these initial conditions (ICs) are set up, we can induce a perturbation to the system. In this section, we apply three types of perturbations to these ICs: a distant and small impact (Sect. 2.1), a generalized small impact (Sect. 2.2), and a large impact (Sect. 2.3). Each perturbation generates a distinctive kinematic signal that we aim to understand in this work.

2.1. Distant and small impacts

To simulate a weak and distant impulsive encounter, we employ the impulse approximation (the perturber passes quickly) and the tidal approximation (the perturber is distant). The form of the resulting velocity kick is derived by integrating the tidal force felt by disc stars over the brief encounter period. Since the tidal force is linear in position and has a two-fold ($m = 2$) azimuthal symmetry, the resulting velocity change is (e.g. Aguilar & White 1985; Struck et al. 2011, A22):

$$\Delta V_R = \epsilon R \cos(2\phi), \quad \Delta V_\phi = -\epsilon R \sin(2\phi), \quad (2)$$

which are added to the ICs defined in Eq. 1. The scale parameter ϵ , that has units of $\text{km s}^{-1} \text{ kpc}^{-1}$, sets the amplitude of this initial velocity kick. For a quick flyby by a mass M_p at closest distance r_p with velocity v_p , ϵ can be estimated as $\epsilon \approx 2 G M_p / (r_p^2 v_p)$ (Sect. 8.2.1. in Binney & Tremaine 2008). In this section, we assume a small impact, $\Delta V_R, \Delta V_\phi \ll V_c$, which requires a small ϵ . The mentioned two-fold symmetry introduced by the perturbation in the radial (ΔV_R) and azimuthal (ΔV_ϕ) velocity fields can be seen in the leftmost panels of the upper rows in Fig. 1.

After evolving these initial conditions for 0.4 Gyr, two distinct wave modes emerge in the velocity field. These are clearly

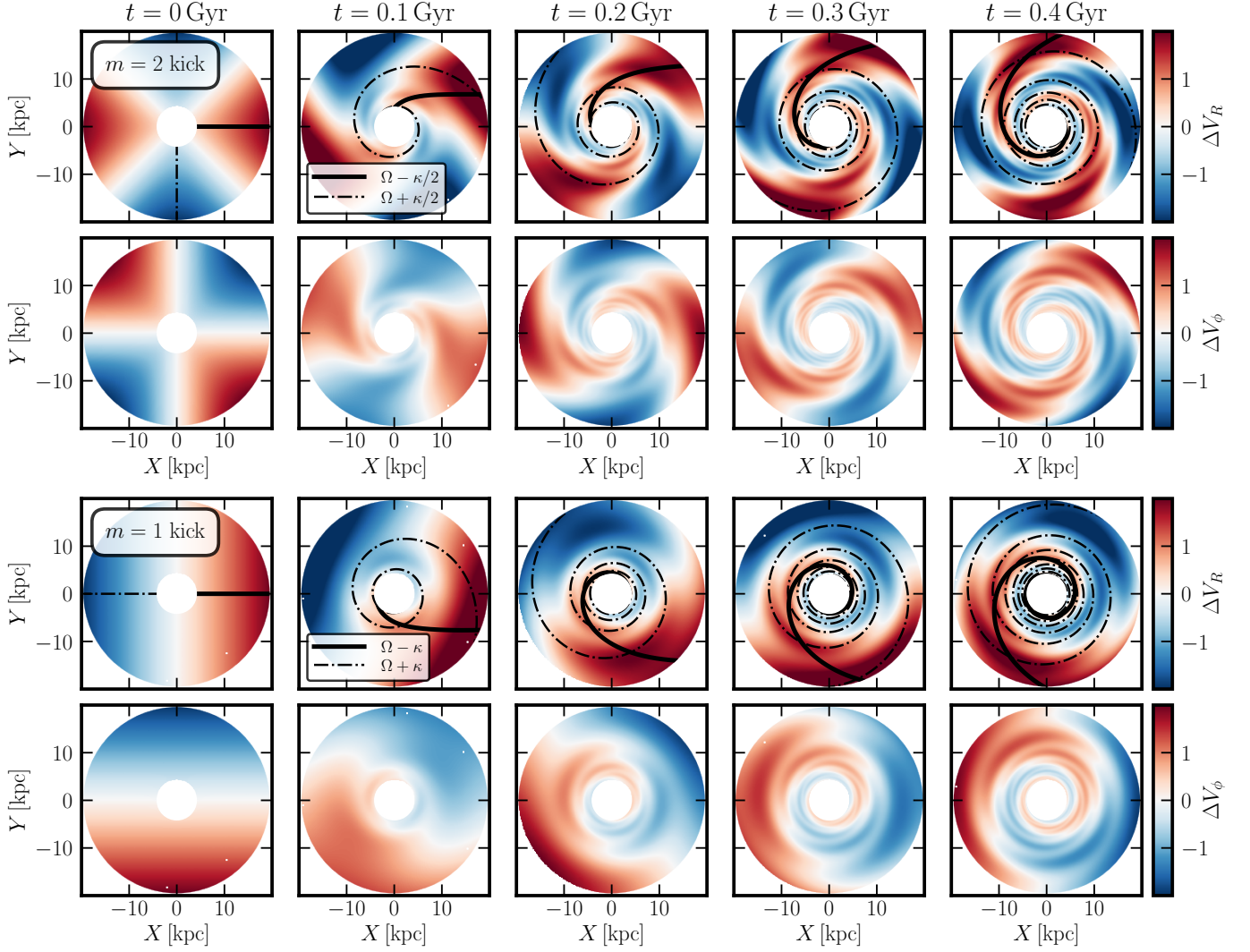


Fig. 1. Kinematic signature evolution of the $m = 2$ (upper panels) and $m = 1$ (lower panels) kinematic kicks. We show snapshots of the velocity perturbation fields at five different times ($t = 0, 0.1, 0.2, 0.3$, and 0.4 Gyr). For each kick mode, the top row displays the radial velocity perturbation, ΔV_R , while the bottom row shows the azimuthal velocity perturbation, ΔV_ϕ . The solid and dash-dotted curves overlaid on the ΔV_R panels indicate the theoretical spiral loci wrapping at pattern speeds $\Omega - \kappa/m$ and $\Omega + \kappa/m$, respectively. The panels demonstrate the clear appearance of two spiral wave patterns for both $m = 2$ and $m = 1$ modes, with the theoretical loci accurately matching the observed evolution of the waves in the velocity fields.

visible in the top rows of Fig. 1, which show the velocity evolution from left to right. The primary wave is seen mostly in the wrapping of the velocity patterns in a spiral shape (red-blue) of large scale. This leads to a density enhancement in regions of negative V_R that constitute the spiral arms (see Fig. 4 in A22). The secondary wave is fainter and wraps faster, so it is seen as smaller scale oscillations on top of the main pattern. Further details and visualizations of the resulting 1D radial profiles, illustrating the contributions of the primary and secondary waves, are presented in Appendix A.

We see that the pattern speed of the primary spiral wave is $\Omega - \kappa/2$, which is widely known and reported in the literature (e.g. Kalnajs 1973; Oh et al. 2008, 2015; Struck et al. 2011), although it has been seen that the presence of a bar or self-gravity can modify this pattern speed, up to $\Omega - \kappa/4$ (e.g. Oh et al. 2015; Pettitt & Wadsley 2018). On the other hand, in A22, we already noted the presence of the secondary wave but we did not characterise it. We see here that it wraps as $\Omega + \kappa/2$ and in Sect. 4 we

give the analytical explanation for its appearance and its wrapping frequency.

2.2. Generalised kinematic kick

The framework described in the previous section assumes an $m = 2$ kinematic kick, but we can extend this formulation to include other shapes of the perturbation, accounting for more complex patterns with multiple m modes from more realistic galactic encounters and halo misalignments (e.g. Chakrabarti & Blitz 2009; Ghosh et al. 2022). Here, we apply idealized m -mode kinematic kicks as a controlled experiment to isolate the dynamical response to specific shapes of the ICs. Specifically, we can generalise Eq. 2 to

$$\Delta V_R = \sum_m \epsilon_m R \cos(m\phi), \quad \Delta V_\phi = - \sum_m \epsilon_m R \sin(m\phi). \quad (3)$$

In the bottom group of Fig. 1, we show the velocity maps for $m = 1$ kick parameters. In this case, the two waves wrap at frequencies of $\Omega_{\text{sp}} = \Omega \pm \kappa$. In general, for every m -shaped kick we

include, two spiral patterns emerge, wrapping according to the relation:

$$\Omega_{\text{sp}} = \Omega \pm \kappa/m. \quad (4)$$

The basic intuition is as follows: each star circles around its reference (guiding) orbit at an angular rate Ω and, in addition, executes small radial (epicyclic) oscillations at a frequency κ . A single star completes one full radial oscillation—reaching repeatedly its apocentre—at this epicyclic frequency κ . However, the imposed m -fold symmetry in the initial perturbation sets the number of apocentres in a given radius. Instead of observing one apocentre per full κ epicycle, the symmetry causes the collective apocentre pattern to repeat every κ/m . Therefore, between two consecutive apocentres of a single star, one observes additional apocentres from other stars — a total of m , spread evenly across the circle. This sets the precession rate, creating the pattern described in Eq. 4.

At a fixed radius, the amplitudes of the primary wave ($\Omega - \kappa/m$) and the secondary wave ($\Omega + \kappa/m$) remain constant in time and are independent of the azimuthal number m . Their relative strength, however, varies with radius and with the choice of gravitational potential. In our fiducial model we have measured the relative amplitude of both waves by computing the 2D Fourier amplitude in $\phi - t$ maps. The ratio of amplitudes between both waves stays nearly constant throughout the disk, taking a value very close to

$$\frac{\mathcal{A}_{\Omega-\kappa/m}}{\mathcal{A}_{\Omega+\kappa/m}} \approx 5.2. \quad (5)$$

where \mathcal{A} represents the amplitude of a wave. In Section 4, we recover this value operating analytically from first principles.

2.3. Single-wave large impacts

While the generalized kinematic kick framework in Sect. 2.2 assumes small perturbations that excite two modes (as shown in Sect. 2.1 and derived analytically in Sect. 4), we now explore regimes where the velocity kick amplitude D (analogous to ϵ , but not restricted to small values) becomes significant. For these large impact simulations, we only study the dynamics of the slow wave, which has a larger amplitude. In addition, the subdominant wave phase-mixes much faster and its long-term contribution is minor. This simplifies the dynamical system and facilitates the application of our data-driven discovery methodology later on. To achieve this, we introduce a specific velocity kick designed to preferentially excite one spiral mode over the other, using a γ -dependent scaling between its radial and azimuthal components:

$$\Delta V_R = DR \cos(m\phi), \quad \Delta V_\phi = -\frac{D}{\gamma} R \sin(m\phi), \quad (6)$$

where $\gamma \equiv 2\Omega/\kappa$ is derived from the potential. Physically, this γ -dependent correction to the azimuthal velocity component balances the two effective restoring coefficients in a disk (κ for radial oscillations and 2Ω for azimuthal ones) so that all stars have the same epicyclic amplitude in the radial and azimuthal direction and uniform phase distribution (Chapter 3.2.3. in Binney & Tremaine 2008). We emphasise again that the emergence of this cleaner, single-wave pattern (Fig. 2) is an intended outcome of our simulation, designed to facilitate the discovery of its governing dynamics using SINDy (Sect. 3.3).

In Fig. 2 we show the full two-dimensional evolution of the system following this impact. As a result of the γ correction,

only a single m -armed spiral pattern emerge, which winds up at the expected rate $\Omega - \kappa/m$. However, the nonlinearity introduced by the large D amplitude generates a non trivial pattern: regions of negative V_R become progressively confined into tighter arcs, while the V_ϕ map develops sharp sign changes.

We can intuitively explain these non-linear wrapping patterns. At a given radius R , the minimum V_ϕ corresponds to the apocentre of an inner orbit with guiding radius $R_{g,\text{in}} < R$. As we discussed in the previous section, the pattern speed of these apocentres locus is $\Omega(R_{g,\text{in}}) - \kappa(R_{g,\text{in}})/m$, and this happens to be larger than $\Omega(R) - \kappa(R)/m$. The opposite argument can be done for the maximum V_ϕ , which correspond to the pericentre of an outer orbit. Therefore, at a given R , the points with minimum (maximum) V_ϕ wrap faster (slower) than the rest, producing these sharp sign changes. This differential wrapping is a general feature of any perturbation, but in the case of large impacts, the amplitude of the velocity oscillations is substantial enough to make these sharp changes visually prominent. In Sect. 4, we use this intuition to find particular PDE coefficients for the large impact case.

These sharp winding features in Fig. 2 are also clearly seen in the one-dimensional $R-V_R$ and $R-V_\phi$ velocity curves at a given azimuth in Fig. 3. In these cuts a clear triangular-wave oscillation appears in V_R , while the V_ϕ profile takes on a sawtooth shape (solid black curves, similar to those described in A22). The overlaid dashed blue line traces the exact form expected in the linear limit (upscaled from the small-impact case in Sect. 2.1), emphasizing how even strong perturbations have comparable pattern speed and overall wave shape, but with the mentioned non-linear effects that we further derive and discuss below (Sect. 4.2). In addition, these 1D projections serve as a better comparison with the *Gaia* data, which are the ones usually plotted for the part of the Galaxy that is observed, and resemble some of the observed features in the $R-V_R$ and $R-V_\phi$ diagrams.

3. Dynamical Discovery with SINDy

In this section, we use the simulations of tidal spiral arms described above, and study them as temporal series to (re-)discover functional forms of equations that govern the system.

3.1. SINDy

SINDy (Brunton et al. 2016) is a data-driven method that extracts the governing equations of a dynamical system directly from measured or simulated data. It is based on the idea that even highly non-linear systems can often be described by equations with only few dominant terms.

For example, a standard linear ODE system is given by

$$\frac{d\mathbf{x}}{dt}(t) = \Theta \mathbf{x}(t), \quad (7)$$

where $\mathbf{x}(t)$ is the state vector and Θ is a constant matrix that characterizes the system dynamics. In practice, SINDy extends this framework to non-linear systems by constructing a library $\mathbf{x}(t)$ of non-linear candidate functions (e.g. polynomials, trigonometric functions, etc) and then uses sparse regression to identify the key terms that govern the behaviour. This approach yields a parsimonious model that preserves the physical interpretability of the dynamics of the system. Importantly, the output of SINDy is limited to the terms provided in its library, and identifies the best fit among these terms rather than discovering arbitrary physical laws.

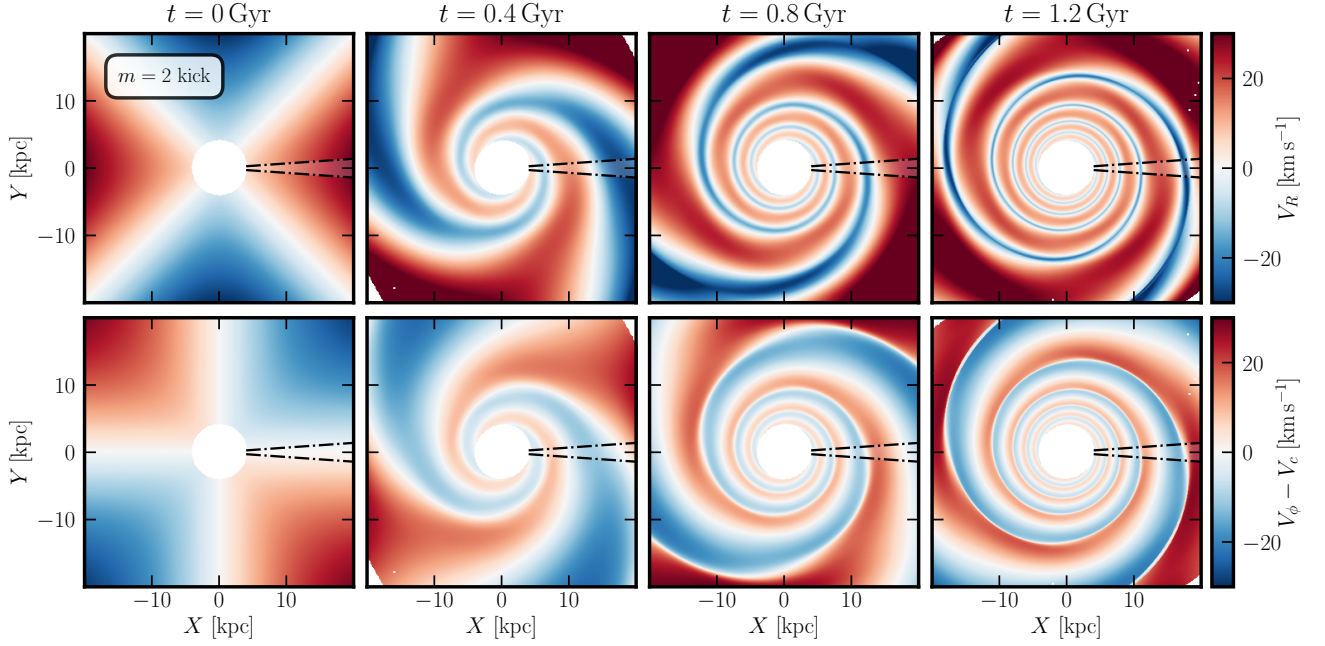


Fig. 2. Evolution of the test-particle system after a large, $m = 2$ impact, designed with a γ correction (Eq. 6) to excite a single spiral pattern. These panels show snapshots of the velocity field at four different times ($t = 0, 0.4, 0.8$, and 1.2 Gyr). The top row shows the radial velocity V_R , and the bottom row shows the residual azimuthal velocity, $\Delta V_\phi = V_\phi - V_c$. The spiral pattern winds up over time at the expected rate $\Omega - \kappa/m$. The large amplitude of the perturbation introduces non-linear effects, causing the regions of negative V_R (blue) to become more concentrated into arcs, and producing sharp sign changes in ΔV_ϕ . One-dimensional radial profiles extracted from these maps along $\phi = 0^\circ$ (dash-dot regions) are presented in Figure 3.

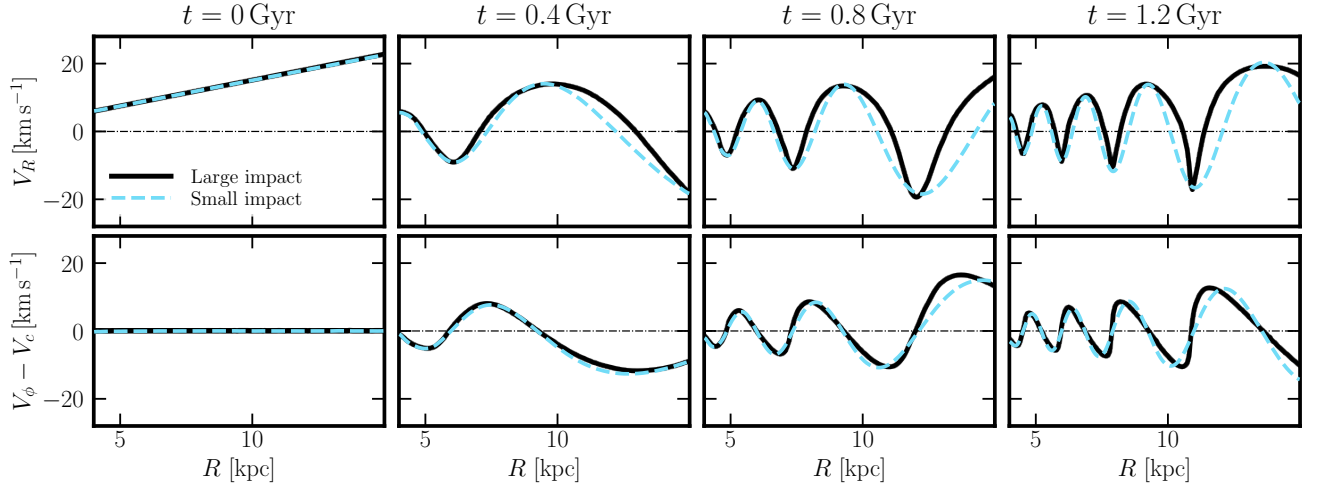


Fig. 3. One-dimensional radial profiles of the velocity perturbations resulting from the large, $m = 2$ impact simulation shown in Figure 2. These profiles show V_R (top row) and ΔV_ϕ (bottom row) as a function of radius R , at the same four times ($t = 0, 0.4, 0.8$, and 1.2 Gyr). The profiles are averaged on small radial bins at fixed azimuth ($\phi = 0^\circ$, corresponding to the dashed-dot regions in Figure 2). The solid black lines represent the results from the large impact simulation. The dashed blue lines show the velocity profiles resulting from the dominant $\Omega - \kappa/m$ wave (specifically the $\Omega - \kappa/2$ wave for $m = 2$) in a small impact simulation (extracted from the blue curves in Fig. A.1), scaled up for comparison. These black 1D profiles reveal the characteristic triangular wave shape in V_R and the sawtooth pattern in ΔV_ϕ , which are key signatures of the non-linear velocity structures generated by the large initial perturbation.

While originally designed for ODEs ($\dot{\mathbf{x}} = f(\mathbf{x})$), the core sparse regression idea extends to PDEs $u_t = N(u, u_x, u_{xx}, \dots)$ by utilizing spatial-temporal data (Rudy et al. 2017; Schaeffer 2017). The process involves numerically computing the time derivative (u_t) and relevant spatial derivatives (e.g. u_x, u_{xx}) from the measured field $u(x, t)$ across all sampled locations and times. These computed derivatives, along with the non-linear combinations of the variables in u , form the library of candidate terms for the right-hand side of the PDE. Conceptually, this treats the

time evolution observed at each spatial location as a distinct data trajectory, and the spatial derivative terms in the library provide the coupling between these locations. A summary and example of the methodology is shown in the diagram of Fig. 4, applied to the Navier-Stokes PDE.

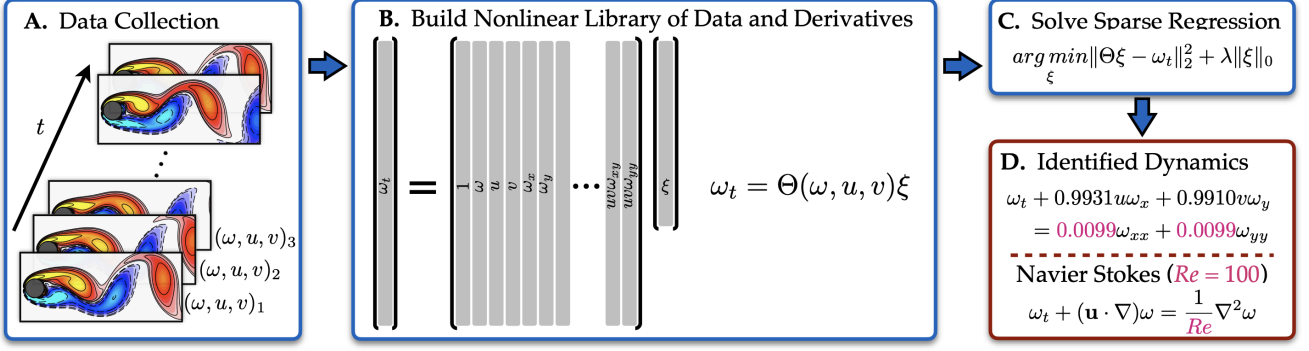


Fig. 4. Schematic example of the usage of SINDy to infer the Navier-Stokes equation in a simulation. A. Collect snapshots representing the solution of the PDE. B. Compute numerical derivatives and organize the data into a comprehensive matrix Θ that includes the candidate terms for the PDE. C. Employ sparse regression techniques to isolate the active terms in the PDE. D. Active terms in the library ($\mathbf{x}(t)$, in the text) are informative of the underlying PDE. Reproduced from Brunton & Kutz (2023), who adapted it from Rudy et al. (2017).

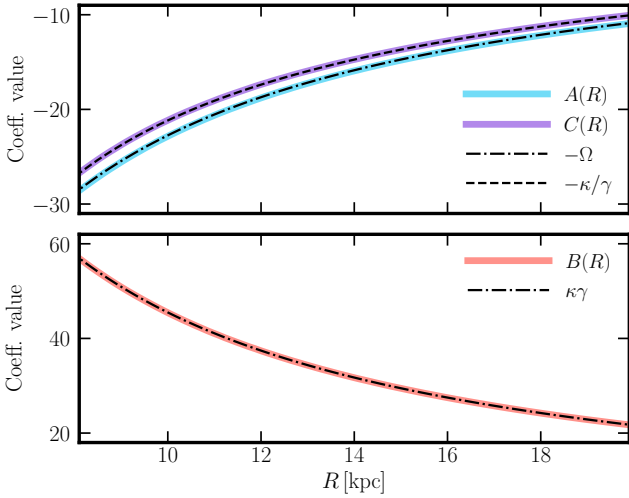


Fig. 5. Radial profiles of the coefficients A (blue), B (coral), and C (purple) from the linear PDE system (Eq. 9) found by SINDy, governing the evolution of velocity perturbations in small impact simulations (Eq. 3). The black lines show the corresponding analytical values derived in Sect. 4 (Eq. 11). The excellent agreement between the SINDy-discovered coefficients and the analytical predictions demonstrates the success in recovering the underlying linear dynamics.

3.2. Equations for the small impact evolution

We now use the simulations of small impacts described in Sect. 2.1 and 2.2 as input for the SINDy PDE method. These simulations were generated using different initial kinematic kicks (corresponding to varying ϵ_m in Eq. 3) with identical results. Thus, the results of this section are independent of the shape of the initial kick, as long as ϵ_m is small.

We treat the velocity perturbations, ΔV_R and ΔV_ϕ , as spatial and time dependent fields, $u(R, \phi, t) = (\Delta V_R, \Delta V_\phi)$. To apply the SINDy PDE approach, we compute the spatial derivatives ($\partial u / \partial R$, $\partial u / \partial \phi$) numerically from the simulation data across all sampled positions and times¹. Our library is composed of polynomial combinations, up to second order, of the state variables

¹ Spatial derivatives were computed numerically by fitting a polynomial of order 3 in a window of 200 pc in the radial direction, and 6° in the azimuthal direction.

and their spatial derivatives:

$$\mathbf{x}(t) = \left(\Delta V_R, \Delta V_\phi, \frac{\partial V_R}{\partial R}, \Delta V_R \Delta V_\phi, (\Delta V_\phi)^2, \dots \right), \quad (8)$$

resulting in a library $\mathbf{x}(t)$ of 36 terms. SINDy is then used to identify the sparse combination of candidate terms that best approximates the measured time derivatives across the entire dataset. Since the underlying gravitational potential is axisymmetric, we expect the coefficients of the governing equations to be independent of ϕ , and depend only on R . To capture this, we run SINDy separately at each radial bin (R). For each radial bin, we combine the data from all ϕ locations within that bin (across all times) to build the SINDy regression problem, allowing us to determine coefficients specific to that radius.

SINDy consistently identified that the dynamics are best described by a linear coupling between the velocity components and their ϕ -derivatives. Specifically, the approach yielded the following equations:

$$\begin{aligned} \frac{\partial \Delta V_R}{\partial t} &= A(R) \frac{\partial \Delta V_R}{\partial \phi} + B(R) \Delta V_\phi \\ \frac{\partial \Delta V_\phi}{\partial t} &= A(R) \frac{\partial \Delta V_\phi}{\partial \phi} + C(R) \Delta V_R \end{aligned} \quad (9)$$

where $A(R)$, $B(R)$, and $C(R)$ are numerical coefficient curves extracted by SINDy at each radial bin. Fig. 5 shows in colours the numerical profiles of these curves (along with a spoiler of the theoretical values we find in Sect. 4). We tested the approach with a variety of potentials and ICs, and observed that the extracted $A(R)$, $B(R)$, and $C(R)$ curves are robust against the different m modes, but do depend on the underlying potential shape. The match between the left side (temporal derivatives) and right side (SINDy library) of both lines in Eq. 9 is excellent ($r^2 \sim 1$), thus showing that SINDy perfectly recovers the governing equations of this system, which motivates our analytical interpretation in Sect. 4.

3.3. Equations for the large impact

We now perform the SINDy analysis for the large impact simulations (Sect. 2.3, Fig. 2). In this case, where small deviations close to equilibrium can no longer be assumed, we apply SINDy directly to the velocity fields, V_R and V_ϕ . The library $\mathbf{x}(t)$ is thus constructed using V_R , V_ϕ , their spatial derivatives ($\partial / \partial R$ and $\partial / \partial \phi$), and all their second-order polynomial combinations, resulting also in 36 terms.

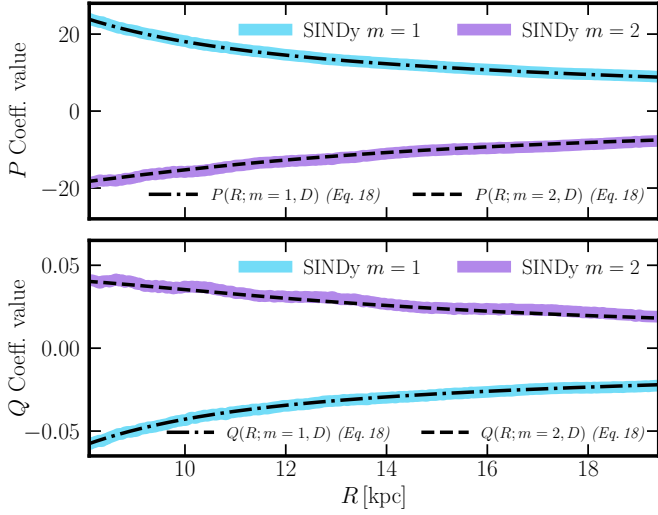


Fig. 6. $P(R; m, D)$ and $Q(R; m, D)$ coefficients found by SINDy for the large impact (Eq. 10) and the corresponding analytical value (Sect. 4.2, Eq. 18). Since the solution depends on m and D , here we show examples for $D = 0.4$ and $m = 1$ (purple) and $m = 2$ (blue).

From this system, SINDy extracts a system of equations with a different combination of parameters:

$$\begin{aligned} \frac{\partial V_R}{\partial t} &= P(R; m, D) \frac{\partial V_R}{\partial \phi} + Q(R; m, D) V_\phi \frac{\partial V_R}{\partial \phi}, \\ \frac{\partial V_\phi}{\partial t} &= P(R; m, D) \frac{\partial V_\phi}{\partial \phi} + Q(R; m, D) V_\phi \frac{\partial V_\phi}{\partial \phi} \end{aligned} \quad (10)$$

where $P(R; m, D)$ and $Q(R; m, D)$ are numerical coefficients, shown in Fig. 6. Again, the fitting between both sides (temporal derivatives vs SINDy library) of the equation is excellent ($r^2 \sim 1$), showing that we are capturing all the dynamics of the system. These coefficients depend not only on the radius and potential but also on the characteristics of the initial impact, namely its shape (mode m) and strength (D), as shown in Fig. 6, where $m = 1$ (blue) coefficients are different than the $m = 2$ ones (purple). Consequently, the coefficients in equations (Eq. 10) are specific to the dynamics established by the initial impact parameters (m, D). This means that the method captures the dynamics of a particular impact rather than revealing a universal governing equation valid for all large impacts. In Sect. 4.2, we exploit the simple quasilinear structure of Eq. 10 to describe it analytically.

4. Interpreting tidal spirals through the learned equations

In the previous section, we found equations describing the evolution of tidal spirals resulting from small (Eq. 9) and large impacts (Eq. 10). SINDy functions provide candidate mechanisms that can then be further analysed and justified through additional experimentation and reasoning. In this way, SINDy serves as a tool to guide us in developing enhanced models and identifying relevant physical mechanisms.

4.1. Small impact equations

For small impacts, the linear PDE system (Eq. 9) can be derived from linearising the Jeans equations, derivable from the Collisionless Boltzmann Equation (CBE). A complete derivation of

this system is given in Appendix B. We reproduce here the resulting linear PDE system for convenience:

$$\begin{aligned} \frac{\partial \Delta V_R}{\partial t} &= -\Omega \frac{\partial \Delta V_R}{\partial \phi} + \kappa \gamma \Delta V_\phi, \\ \frac{\partial \Delta V_\phi}{\partial t} &= -\Omega \frac{\partial \Delta V_\phi}{\partial \phi} - \frac{\kappa}{\gamma} \Delta V_R. \end{aligned} \quad (11)$$

These reveal the analytic explanation of the coefficient curves obtained by SINDy in Eq. 9:

$$A(R) = -\Omega, \quad B(R) = \kappa \gamma, \quad C(R) = -\frac{\kappa}{\gamma}. \quad (12)$$

In Fig. 5, we show these analytical values on top of the SINDy results.

Equation 11 is equivalent to Eqs. 2b and 2c in Lin & Shu (1964) and Eqs. 10 and 11 in Toomre (1964). In those equations there is an extra term in the right side of the equations depending on the perturbed component on the potential, Φ' , that here we fixed to be zero. The PDE system is nearly the same, but the problem we are studying is different. In Lin & Shu (1964) and Toomre (1964), the question was how the perturbed potential Φ' propagates through self-gravity, assuming equilibrium ICs in velocity. We take a very different approach, where we neglect self-gravity and impose an initial kinematic kick.

Solving this system analytically yields solutions in the form of spiral kinematic waves (see Appendix B.2 for a complete derivation). This solution consists of a sum of waves with frequencies $\omega = m\Omega \pm \kappa$:

$$\begin{aligned} \Delta V_R(R, \phi, t) &= \sum_m \left[a_m e^{i(m\phi - (m\Omega + \kappa)t)} + b_m e^{i(m\phi - (m\Omega - \kappa)t)} \right], \\ \Delta V_\phi(R, \phi, t) &= \sum_m \left[c_m e^{i(m\phi - (m\Omega + \kappa)t)} + d_m e^{i(m\phi - (m\Omega - \kappa)t)} \right], \end{aligned} \quad (13)$$

where a_m, b_m, c_m, d_m are amplitudes determined by the initial conditions, and $c_m = -\frac{i}{\gamma} a_m$, $d_m = \frac{i}{\gamma} b_m$. These waves wrap at pattern speeds

$$\Omega_p = \Omega \pm \frac{\kappa}{m}, \quad (14)$$

demonstrating the relation (Eq. 4) that we discussed in Section 2.2. This solution provides an explicit, closed-form description of the temporal evolution of the residual velocities, setting the stage for interpreting the underlying dynamics.

Building on the analytical solution (Eq. 13), we now focus on the impulsive and weak interaction, $m = 2$, case (Struck et al. 2011), discussed in Section 2.1. Applying those ICs (Eq. 2) to this analytical framework reveals that the initial impulsive encounter naturally decomposes into two wave modes wrapping at pattern speeds $\Omega \pm \kappa/2$. In Appendix B.3 we show the detailed derivation which, in addition, indicates that the relative amplitudes of these two modes are directly determined by the potential properties by:

$$\frac{\mathcal{A}_{\Omega - \kappa/2}}{\mathcal{A}_{\Omega + \kappa/2}} = \frac{|b_2|}{|a_2|} = \frac{1 + \gamma}{\gamma - 1}. \quad (15)$$

For our fiducial potential, $\gamma \sim 1.46$ across all the disk. This gives an amplitude ratio of ~ 5.34 , very similar to the empirical measurement we provided in Sect. 2.2 (Eq. 5). The 1D velocity profiles, showing the relative dominance of the $\Omega - \kappa/2$ mode and the fainter $\Omega + \kappa/2$ oscillations, are shown in Fig. A.1.

4.2. Large impact equations

Here we analyse the non-linear PDE (Eq. 10) discovered by SINDy in the large impact simulation. Unlike in the small impact case where the SINDy-discovered linear system (Eq. 9) directly corresponds to the linearized Jeans equations, the non-linear PDE (Eq. 10) found for the large impact is, as discussed in Sect. 3.3, specific to the ICs and not a general law. Consequently, we do not expect it to be derivable from first principles in the same straightforward way. Here we focus on interpreting the dynamics directly through the structure of the PDE identified by SINDy for this particular type of strong perturbation.

We focus our analytical analysis on the azimuthal equation because its structure is “self-contained”, meaning its form depends only on V_ϕ and its spatial derivatives, allowing us to determine the evolution of V_ϕ independently of V_R . SINDy found that both equations in the system (Eq. 10) share the same coefficients, P and Q . This means that we can derive these key coefficients, applicable to both velocity components, by analysing only one of the equations.

The azimuthal part of Eq. 10 is of the first-order quasilinear type and is naturally solved by the method of characteristics. This means that the quantity V_ϕ remains constant along characteristic curves defined by

$$\frac{d\phi}{dt} = P(R; m, D) + Q(R; m, D)V_\phi, \quad \frac{dV_\phi}{dt} = 0. \quad (16)$$

We have already discussed the existence of these characteristic curves. In Sect. 2.3 we explained that, at each R , the minimum V_ϕ corresponds to the apocentre of an inner orbit with guiding radius $R_{g, \text{in}}$, and moves at a constant pattern speed $\Omega(R_{g, \text{in}}) - \kappa(R_{g, \text{in}})/m$. An equivalent reasoning brings us to the conclusion that the points where $V_\phi = V_c$ move at a constant pattern speed $\Omega(R) - \kappa(R)/m$.

These associations provide two constraints on the coefficients P and Q . By equating the instantaneous pattern speed from the characteristic curve (Eq. 16) to the expected pattern speed for two specific constant V_ϕ values, we arrive at the following system of equations:

$$\begin{aligned} P + Q \left(V_c - \frac{D}{\gamma} R \right) &= \Omega(R_{g, \text{in}}) - \frac{\kappa(R_{g, \text{in}})}{m}, \\ P + Q V_c &= \Omega(R) - \frac{\kappa(R)}{m}. \end{aligned} \quad (17)$$

where the first equation corresponds to the apocentres ($V_\phi = V_c - DR/\gamma$, minimums in Eq. 6), that evolve with pattern speed $\Omega(R_{g, \text{in}}) - \kappa(R_{g, \text{in}})/m$ and the second equation corresponds to points where $V_\phi = V_c$, with pattern speed $\Omega(R) - \kappa(R)/m$.

Solving this linear system for P and Q , we obtain a closed formula for the PDE coefficients

$$\begin{aligned} Q(R; m, D) &= -\frac{\gamma}{DR} \left(\Delta\Omega - \frac{\Delta\kappa}{m} \right), \\ P(R; m, D) &= -\left(\Omega(R) - \frac{\kappa(R)}{m} \right) - QV_c. \end{aligned} \quad (18)$$

where we defined $\Delta\Omega \equiv \Omega(R_{g, \text{in}}) - \Omega(R)$ and $\Delta\kappa \equiv \kappa(R_{g, \text{in}}) - \kappa(R)$. In Fig. 6, we show that these curves match perfectly with the coefficients extracted by SINDy, providing strong validation for both the SINDy discovery and our analytical interpretation based on characteristic curves linked to orbital behaviour.

Crossing time The characteristic curves of the system reveal an important dynamical aspect: the eventual crossing of the characteristic curves. In the astrophysical context, this corresponds to the appearance of overlapping kinematic populations in the same spatial volume, which challenges the definition of a unique “mean velocity” and, ultimately, the assumptions in the Jeans equations.

From Zachmanoglou & Thoe (1986), we can extract that, for a PDE with the shape of Eq. 10, this overlap or crossing time is:

$$t_{\text{cross}} = -\frac{1}{Q_{m,D}(R) V'_{\phi,0}(\phi_c)} \quad (19)$$

meaning that the earliest crossing originates at the point ϕ_c where the derivative of the initial condition $V_{\phi,0}$ (Eq. 6) is the most negative. Operating this equation gives us a closed expression for the earliest crossing time

$$t_{\text{cross}} = \frac{1}{m\Delta\Omega - \Delta\kappa}. \quad (20)$$

Even in simulations where the Sgr impact on the velocities at the Solar neighbourhood is on the larger side of the spectrum ($\Delta V_R, \Delta V_\phi \sim 25 \text{ km s}^{-1}$), this would translate to $D \sim 2$. In our framework, this yields $t_{\text{cross}} \gtrsim 1.5 \text{ Gyr}$, comfortably exceeding the estimate of the last Sgr passage ($\lesssim 1 \text{ Gyr}$). Indeed, Hunt et al. (2024) studied the kinematics of radial phase mixing and found $\Delta R - V_R$ phase spiral patterns and showed that, for a kick compatible with a Sgr passage, the wraps of the radial phase spiral appear at least after $\sim 1 \text{ Gyr}$. Thus, in the context of a Sgr passage, we do not expect a crossing of the perturbed populations.

5. Applying SINDy to more realistic simulations

We do one last exercise towards the generalisation of this method, applying it to a more realistic model. We use a N -body simulation of a Sgr-like impact and a test-particle rerun (TPR) of the same simulation (Asano et al. 2025, Asano et al., in prep.), initialized with particles from the same snapshot but evolved in a fixed axisymmetric potential. Running SINDy on these models allows us to test the capacity of the method in more complex 3D setups with velocity dispersion and self-gravity effects. Details of these simulations can be found in Appendix D.

Figure 7 shows the velocity maps for the N -body (first and third columns) and TPR (second and fourth columns) models over a $\sim 250 \text{ Myr}$ period after the first Sgr pericentre. We observe that a clear bar dominates the inner region of the disc ($R < 7 \text{ kpc}$, indicated by the dashed circle), so here we focus our analysis on the outer region ($R > 7 \text{ kpc}$) to study the tidal spiral arms. In this outer region, we see similar patterns to those discussed in Sect. 2.3 with our idealized test particle models with large impact. We observe a winding spiral with pattern speed $\Omega - \kappa/m$, which we measured using Fourier decomposition in these kinematic maps. This spiral pattern also displays characteristic non-linear features: regions with negative V_R (blue) tend to concentrate, and the V_ϕ profile develops sharp edges. These realistic simulations, however, also reveal additional substructure (e.g., thin arches, bifurcations) that differs from the simplified idealized models. Finally, we observe subtle differences between these two models in Fig. 7, primarily a larger amplitude of the kinematic waves in the N -body simulation at $t = 1.15 \text{ Gyr}$ (third and fourth rows). This difference could be related to the self-gravity of the spiral arms and/or the extra acceleration of the perturber after the pericentre, which are not included in the TPR model.

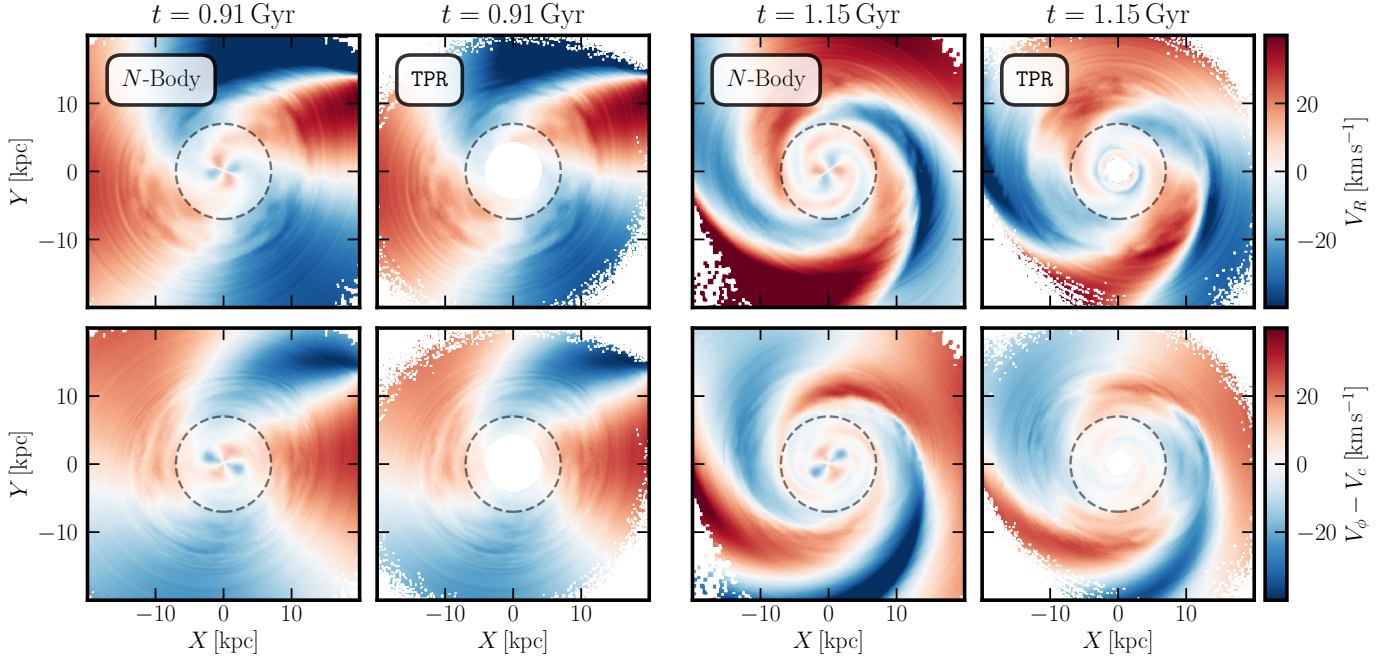


Fig. 7. Kinematic maps comparing the evolution of velocity fields in the *N*-body (first and third columns) and TPR models (second and fourth columns). The panels show snapshots of the radial velocity V_R (top row) and the azimuthal velocity perturbation ΔV_ϕ (bottom row) in the X - Y plane at two different times. The dashed circle denotes the inner region ($R < 7$ kpc) that was excluded from the analysis. Observe the winding of the spiral patterns over time and the overall similarity between the *N*-body and TPR models, with subtle differences, particularly in the amplitude of the kinematic waves.

5.1. SINDy results

Now we apply SINDy to the TPR and *N*-body models. Since we are in the large impact regime, we apply the same strategy as in Sect. 3.3: feeding V_R , V_ϕ , and their spatial derivatives. In both models, from a library of 36 terms, SINDy successfully recovered the exact same structural form of the non-linear PDE (Eq. 10). This striking consistency shows the robustness of the method in identifying the core dynamical relationships, and that the equation form discovered in the ideal models holds beyond the test cases.

In Fig. 8 we show the P (first row), and Q (second row) coefficients obtained by SINDy in the TPR (blue) and *N*-body models (purple), as well as the analytical prediction (Eq. 10). The left (right) column shows the coefficients obtained when fitting the radial (azimuthal) part of the non-linear PDE (Eq. 10). Although the coefficient P should be identical in the radial and azimuthal equations (same for Q), SINDy fits them independently, allowing for different results. The bottom row of Fig. 8 shows the r^2 value. This value indicates how good the SINDy model fits the data at each radius. In both cases, the fit is sub-optimal ($r^2 < 0.7$). This points to missing terms in our library.

For the TPR model (blue lines in Fig. 8), the recovered coefficients match the expected ones (dashed-dot lines, Eq. 18) fairly good, with the exception of some coherent oscillations in R . For the *N*-body simulation (purple lines in Fig. 8), the recovered coefficients are similar to the ones recovered from the TP rerun in the radial equation, but differ significantly in the azimuthal direction. We discuss the possible causes of this deviation in the following section.

5.2. Limitations of the method

The suboptimal r^2 fitting of the coefficients recovered by SINDy in the realistic models (bottom row in Fig. 8) reveals significant limitations in our approach. Compared to the idealized setup (Sect. 2.3), the realistic models introduce complexities such as vertical motion, velocity dispersion, different (more complex) initial conditions, and self-gravity. These factors are potentially responsible for the reduced goodness-of-fit.

Vertical motion Our analysis (Sect. 3.3) uses a 2D model. However, the disc in the TPR and *N*-body models is 3D. We tested the impact of the vertical motion by applying SINDy to a subsample of particles with small $|Z|$ and $|V_Z|$ from the TPR model. The recovered coefficients were nearly identical to those from the full sample. This suggests that, in this specific simulation and time frame, the vertical motion is likely not the primary cause for the suboptimal fit of the equations.

Velocity dispersion In A22 we studied test particle simulations with a significant velocity dispersion, and showed that the pattern speed of the spiral arms and the evolution of the system is very similar to our idealised models. However, the velocity dispersion contributes to the Jeans equations, and can influence the exact shape of the kinematic waves. In addition, the noise that the velocity dispersion introduces is likely to make the precise coefficient recovery difficult by SINDy. Therefore, these two factors likely contribute to the residual error and the suboptimal r^2 values observed in Fig. 8.

ICs The ICs in the realistic models are taken from a simulation snapshot at $t = 0.9$ Gyr, reflecting the full dynamical history (tidal impact, bar, previous spiral arms, etc.). This differs from

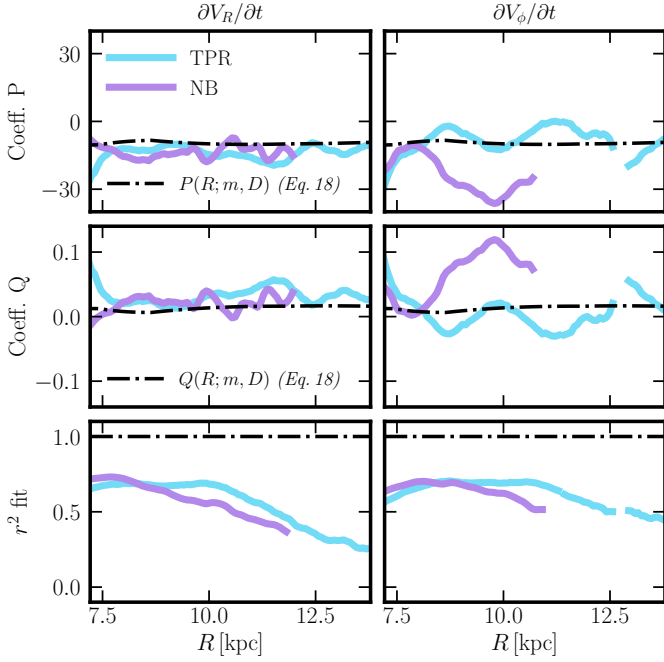


Fig. 8. Results from applying SINDy to the TPR (blue lines) and N -body (purple lines) models. The top row shows the SINDy-recovered coefficient P , and the middle row shows coefficient Q , both as a function of R . The bottom row shows the r^2 value, indicating the goodness-of-fit for the SINDy model at each radius. The black dash-dotted lines represent the analytical predictions for P and Q (Eq. 18). The coefficients P and Q obtained by fitting the radial derivative ($\partial V_R/\partial t$) and the azimuthal derivative ($\partial V_\phi/\partial t$) are shown in the left and right columns, respectively. Voids in the curves correspond to radii where SINDy failed to find a solution.

the idealized analytic kick assumed for the theoretical coefficients (Eq. 6) that determines the values of the $P_{m,D}$ and $Q_{m,D}$ coefficients. Consequently, the recovered coefficients in Fig. 8 are not expected to perfectly match the analytical predictions across all radii.

Self-gravity The main discrepancy between the coefficients extracted from the TPR and N -body models is observed in the azimuthal equation (right column in Fig. 8). We hypothesize that this discrepancy is driven by the self-gravity of the spiral arms. For loosely wound spirals, as in the temporal range we consider (Fig. 7), the self-gravity acceleration is more dominant in the azimuthal direction than in the radial direction (Lin & Shu 1964). It is also important to notice that the radius where the difference between the TPR and N -body coefficients is larger, $R = 10$ kpc, corresponds to the Outer Lindblad Resonance radius of the bar. While this alignment may be coincidental, it raises the possibility that the bar is contributing to the discrepancy between the SINDy results and theoretical predictions.

Missing terms in the library The consistently low r^2 values in Fig. 8 (bottom row) are the strongest indication that the equation discovered by SINDy (Eq. 10) is missing important physics, such as velocity dispersion and self-gravity. While it is difficult to determine the precise contribution of each, these terms are necessary components of the full Jeans equations that govern disc dynamics, and capturing a more complete dynamical de-

scription in the future will require expanding the SINDy library to include them.

6. The $Gaia$ L_Z – $\langle V_R \rangle$ wave

Friske & Schönrich (2019) showed a clear wave in the $L_z - V_R$ projection of the *Gaia* data (studied also in A22, Cao et al. 2024). They found that the wave is composed of a short and a long wavelength pattern with similar amplitudes ($\mathcal{A}_1 = 7.0 \text{ km s}^{-1}$ and $\mathcal{A}_2 = 8.0 \text{ km s}^{-1}$), and differing wavelengths ($\lambda_1 \sim 285 \text{ kpc km s}^{-1}$ and $\lambda_2 \sim 1350 \text{ kpc km s}^{-1}$). The presence of these two waves in the planar motion of the MW, combined with the two wave pattern ($\Omega \pm \kappa/2$) observed in Sect. 2 from a single impact, raises a clear question: could we explain the full L_Z – $\langle V_R \rangle$ wave with a simple impulsive impact like that of a single Sgr passage?

To investigate this, we start by examining the L_Z – $\langle V_R \rangle$ wave in *Gaia* DR3 data² (blue curve in the left panel of Fig. 9). We also plot the mean radial velocity $\langle V_R \rangle$ in the $L_z - \phi$ plane (central panel in Fig. 9, also shown in Chiba et al. 2021, A22). We observe patterns consistent with previous findings, showing diagonal features in the $L_z - \phi$ plane, potentially indicative of spiral structure. We test the simplest scenario that could produce these signatures: a single distant impulsive Sgr passage (Eq. 2). Using the analytical solution (Eq. 13), we constructed $V_R = f(L_Z, \phi; t, \epsilon, \phi_0, V_{R,0})$ to fit the $\langle V_R \rangle$ of the observations. Here, t is the time since the impact, ϵ is the impact strength, ϕ_0 is the initial angle of the perturber, and $V_{R,0}$ is a constant offset in V_R (equivalent to the t parameter in Eq. 2 in Friske & Schönrich 2019). The fit is done by minimizing the squared difference between the model and data³.

The right panel of Fig. 9 shows the best-fit model map in the $L_Z - \phi$ plane, and the purple curve in the left panel shows the corresponding L_z – $\langle V_R \rangle$ profile at $\phi = 0^\circ$, compared to the *Gaia* data (blue curve). The best values we found for the model parameters are:

$$t = 0.42 \text{ Gyr}, \quad \epsilon = 0.61 \frac{\text{km s}^{-1}}{\text{kpc}}, \quad \phi_0 = 78^\circ, \quad V_{R,0} = 6.3 \text{ km s}^{-1}.$$

The values obtained are quite reasonable. For instance, the fitted time t is roughly consistent with estimates for the time of impact derived from fitting the vertical phase spiral (Antoja et al. 2018; Frankel et al. 2023; Antoja et al. 2023; Darragh-Ford et al. 2023). The initial angle ϕ_0 is not well constrained by the fit. For the impact parameter ϵ , which can be approximated by $\epsilon = 2GM_p/(r_p^2 V_p)$ (Sect. 2.1), we see that, using the values for the last pericentre from Vasiliev et al. (2021), $r_p \sim 24.3$ kpc and $v_p \sim 281 \text{ km s}^{-1}$, our fitted value implies a Sgr mass estimate of $M_p \sim 1.17 \times 10^{10} M_\odot$, which is one order of magnitude larger than the total mass estimated at the last pericentre (Vasiliev et al. 2021). The need for a higher mass of Sgr to reproduce the observables has already been pointed out in other studies (e.g. Binney & Schönrich 2018; Laporte et al. 2019). However, these

² We use StarHorse (Anders et al. 2022) distances, and typical quality cuts and Solar parameters. For more details, we refer to Sect. 2.1 in Bernet et al. (2024).

³ To find the optimal values for $t, \epsilon, \phi_0, V_{R,0}$, we run a simple search process. We sample different starting values to help avoid finding only a local best fit, and minimize the squared difference of the histograms (central and right panels in Fig. 9) using the L-BFGS-B implementation in `scipy.optimize` (Virtanen et al. 2020). We used `MilkyWayPotential2022` (Price-Whelan 2017) as the potential for the analytical formulation

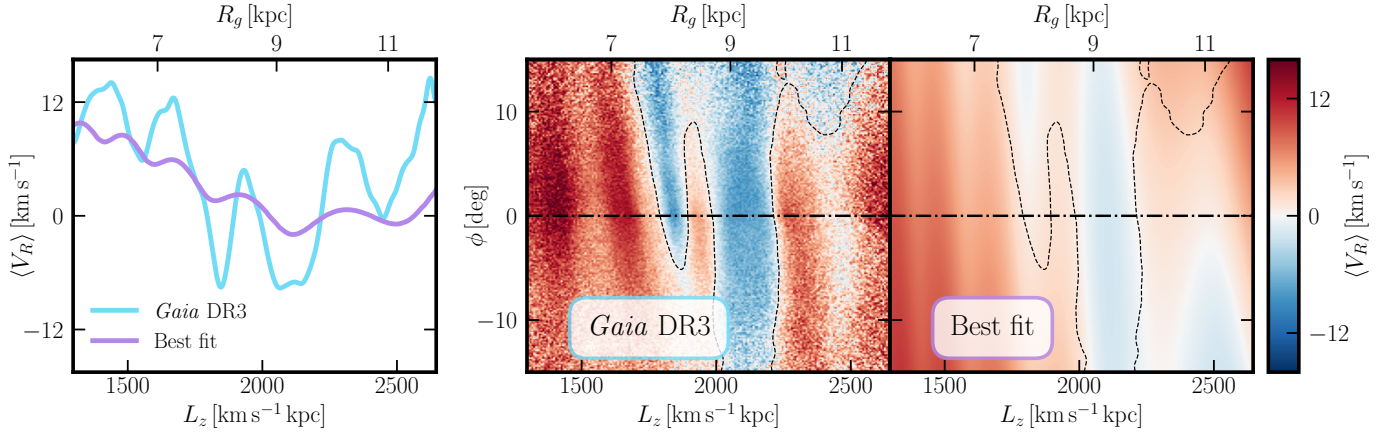


Fig. 9. Best fit of an impulsive $m = 2$ perturbation to the *Gaia* DR3 $L_z - \phi - \langle V_R \rangle$ map. Left panel: $\langle V_R \rangle$ as a function of L_z for *Gaia* DR3 data (blue) and the best fit model (purple), at $\phi = 0^\circ$ (dot-dashed line in the other panels). Middle panel: The $L_z - \phi$ map of $\langle V_R \rangle$ for *Gaia* DR3 data. Right panel: $L_z - \phi$ map of $\langle V_R \rangle$ for the best fit model. The dashed curve indicates the $\langle V_R \rangle = 0 \text{ km s}^{-1}$ curve of the data.

mass estimates remain inconclusive due to the unconstrained mass loss history of Sgr.

More importantly, this model, and thus the obtained parameters, has several limitations. To start with, the impulsive kick model predicts a large amplitude difference between the two waves (~ 5.34 , Eq. 15), while in the *Gaia* data, these amplitudes are much more similar (~ 1.14). This means that the model cannot reproduce the observed balance between the two wave components. This is seen in the difference between the ‘short’ waves in the left panel of Fig. 9. Another limitation is the use of the linear model instead of the non-linear equations. However, for the time and amplitude range of the fitting, we only expect small second-order corrections to the shape of the wave (see central panels of Fig. 3), and thus this would not be a significant issue. Finally, the limitations discussed in Sect. 5.2 also apply here, so accounting for the velocity dispersion or self-gravity effects could influence the fitting results.

In addition, our model is only considering a single, impulsive passage, but could be extended or combined with complementary dynamical processes. These could include the effect of multiple Sgr passages, each one generating one of the observed waves, as we explored in A22: closer non-impulsive perturbations; the combined influence of the Galactic bar and stellar spiral arms (e.g. Hunt et al. 2019; Khalil et al. 2024); or the cumulative effect of other past or present perturbers. Despite all the listed limitations, both the obtained fitting and parameters are promising results, pointing to a potential diagnostic of the Sgr passage using planar motions. We aim to explore this model in detail in future work.

7. Discussion

7.1. Potential of the method

Applying data-driven discovery tools like SINDy to simulations offers significant potential, serving as an empirical guide or providing simplified descriptions in complex regimes. In the case of the small-impact simulations, SINDy identified the linear PDE system described by Eqs. 9 and 11. This system is known in the literature to describe the evolution of perturbations in a collisionless disk (e.g. Toomre 1964; Lin & Shu 1964). The significance here is not the novelty of the equation itself, but the ability of the method to extract this fundamental structure directly from the simulated phase-space data. This success served as a validation

of the SINDy approach for this type of problem and provided the empirical foundation that guided our analytical derivation (Sect. 4), enabling us to obtain explicit, closed-form solutions describing the phase-space distribution at all times (Eq. 13).

For the specific large-impact scenario, SINDy discovered a non-linear PDE system (Eq. 10) governing the kinematic perturbations. To our knowledge, this particular form has not been explicitly discussed previously in the context of galactic dynamics. Although this equation is specific to the used ICs and not a general law like the Jeans equations, its surprising simplicity – notably the absence of explicit radial derivatives and a single non-linear term – contrasts with the complexity of the full Jeans equations required to model this regime. This simpler structure directly facilitated the theoretical analysis of features like the characteristic curves and the derivation of the crossing time (Eq. 20).

Our application of SINDy to more realistic simulations (Sect. 5) underscores the value of this approach. SINDy successfully recovered the same structural form of the non-linear PDE (Eq. 10) that was found in the idealized large-impact simulations. Thus, the method proves robust even in the presence of velocity dispersion, 3D motion, and a more complex dynamical history. The observed discrepancies in the recovered coefficients (Fig. 8) are not necessarily a failure, but rather a valuable outcome: they point to the physical effects (like self-gravity, as discussed in Sect. 7.2) that are missing from the current simplified model and need to be incorporated into the SINDy library for a more complete description. This demonstrates how data-driven discovery can guide the systematic inclusion of physical processes in dynamical models.

The governing PDEs we have identified also open up a route for efficient forward modelling. Instead of running full particle simulations or numerically solving PDEs directly, one can transform the PDEs into systems of coupled ODEs by expanding the dynamical fields in a basis of functions. This approach, characteristic of spectral methods, allows for faster evolution of the system in coefficient space, and is closely related to the latest developments in galactic dynamics (Roziar et al. 2019; Petersen et al. 2024). We demonstrate this technique for the linear PDE system and show its effectiveness in Appendix C. While more complex for the non-linear case, solving the resulting ODE system still offers significant computational advantages over traditional methods.

7.2. Adding self-gravity to the mix

Our current simplified PDE (Eq. 10) does not explicitly include terms representing the self-gravitational forces or the potential response of the live halo (Bernet et al. 2025). This introduced discrepancies when applying SINDy to more realistic simulations (Sect. 5, Fig. 8). The data-driven discovery framework, however, offers clear paths to address these limitations. One approach is to explicitly calculate the gravitational acceleration due to the evolving self-consistent density structure of the spiral arms (and potentially other components like the live halo or external perturber). These calculated accelerations could then be included as additional terms in the SINDy library, treating the self-gravity as an external force acting on the system.

Another clear path to extend the SINDy library is to include terms related to the density field itself. The method could potentially uncover a different, more comprehensive set of PDEs. We hypothesize that SINDy might identify a PDE structure that intrinsically accounts for the self-gravitational forces, potentially finding a more effective or simplified representation than the full, complex Jeans equations required for the coupled density-velocity system. Beyond self-gravity, these data-driven techniques could also prove powerful for uncovering tractable, scenario-specific models of complex effects such as dynamical friction—especially difficult to solve analytically—just as SINDy identified a relatively simple non-linear PDE (Eq. 10) for the large-impact case. In addition, SINDy is closely related to other data-driven dynamical analysis methods, such as Dynamic Mode Decomposition (DMD, Schmid 2010, see Brunton et al. 2016). DMD identifies dominant system modes and has been applied to simulations of vertical phase spirals (Darling & Widrow 2019). While DMD focuses on modes, SINDy aims to find the governing equations, offering a complementary perspective that could also be applied to phenomena like self-gravitating vertical phase spirals.

7.3. Application to observational data

In Section 6, we applied our analytical model for an impulsive kinematic kick (derived from the linear PDE, Eq. 13) to fit the observed $L_Z - \langle V_R \rangle$ wave in *Gaia* data. Fig. 9 shows that this simple model can reproduce the overall structure and winding pattern of the observed wave reasonably well, providing specific parameters for the Sgr passage time and strength, although several key limitations are mentioned.

The idea of analysing kinematic wave structures like the $L_z - V_R$ wave can be generalised to model similar phenomena in external galaxies. The increasingly precise kinematic maps, obtained through integral field spectroscopy (e.g. Erroz-Ferrer et al. 2015; Cappellari 2016; den Brok et al. 2020), and even using *Gaia* data in the LMC (Jiménez-Arranz et al. 2023, 2024, 2025), provide rich datasets of kinematic information. These datasets contain several examples of tidal features and kinematic waves, offering an ideal opportunity to apply the methodology derived in this work to study a large variety of systems.

8. Summary and conclusions

The spiral structure and overall dynamics of the MW remain a major area of research, with recent observations highlighting that the MW disc is not in a steady state but is actively perturbed, likely by the passage of the Sgr dwarf galaxy. In this work, we explored the dynamics of tidally induced spiral arms applying SINDy, a data-driven technique that identifies the governing dif-

ferential equations of a dynamical system directly from simulation data. Our main findings are summarized below:

- A single m -fold impulsive velocity kick with small amplitude triggers the formation of two m -armed spiral waves, wrapping at pattern speeds $\Omega \pm \kappa/m$. The amplitudes of these waves depend on the shape of the initial kick and the potential, and can be analytically described (Sect. 4).
- Applying SINDy to simulations of small impacts, we successfully recovered the linear PDE (Eq. 9) governing the evolution of the system, validating the capability of the method in this context.
- Guided by the SINDy discovery, we analytically re-derived the linear PDE system from first principles using the CBE. This derivation recovers equations equivalent to classical descriptions (Toomre 1964; Lin & Shu 1964) and provides a closed-form solution (Eq. 13) of the temporal evolution of the V_R and V_ϕ maps.
- We defined a family of simplified larger impacts (Eq. 6) resulting in m -armed spiral patterns. For these cases, SINDy discovered a simple, previously unknown non-linear PDE system (Eq. 10), that describes the evolution of the system, demonstrating its potential to uncover simplified governing equations in complex regimes.
- The coefficients of the non-linear PDE (Eq. 10) are specific to the initial impact characteristics (mode m , strength D), highlighting that this equation describes the dynamics for a particular type of perturbation, not a universal law. However, its simple mathematical structure enables the interpretation of its characteristic kinematic features.
- The analysis of the non-linear PDE (Eq. 10) provides a framework for interpreting the characteristic kinematic patterns observed in simulations (e.g. triangular V_R and sawtooth V_ϕ profiles in Fig. 3), which resemble features in MW phase space (like the $R - V_\phi$ ridges and $L_z - V_R$ wave). Our interpretation of this PDE through characteristic curves reveals that these patterns arise from differential wrapping.
- Applying our data-driven framework to more realistic simulations (an N -body simulation and its test-particle rerun), we successfully recovered the same non-linear PDE structure (Eq. 10) found in idealized simulations, demonstrating the potential of this method in more complex setups.
- The coefficients recovered from the realistic simulations showed discrepancies compared to idealized cases (Fig. 8), which we attribute primarily to physical effects not explicitly included in our simplified PDE, such as self-gravity.
- We applied the closed-form solution (Eq. 13), assuming a simple impulsive kick, to fit the *Gaia* $L_Z - \langle V_R \rangle$ wave (Sect. 6). We obtained reasonable visual fit and parameters for a Sgr passage, including a passage time of ~ 0.42 Gyr and an inferred perturber mass $\sim 1.17 \times 10^{10} M_\odot$. However, our model shows a significant discrepancy in the amplitude ratio between the two main observed components, suggesting a more complex origin than a single simple impact.

The evolution of the field of galactic dynamics, increasingly data-driven, demands new methods to study the fundamental principles governing non-equilibrium dynamics. Our approach offers a new path to explore theoretical dynamics often intractable otherwise. It complements other novel data-driven techniques in the field, such as Orbital Torus Imaging (OTI, Price-Whelan et al. 2021, 2025; Horta et al. 2024; Oeur et al. 2025) for constraining the gravitational potential, basis function

expansions (Johnson et al. 2023; Arora et al. 2024, 2025) for efficient dynamical field evolution, and neural network-based potential recovery from kinematics (Green et al. 2023; Kalda et al. 2024; Zucker et al. 2025). These frameworks that link empirical data to predictive analytical models offer a direct path for exploring theoretical dynamics and dissecting complex galactic structure and evolution, including challenging phenomena like self-gravity and dynamical friction.

Acknowledgements. We thank Kathryn V. Johnston, Chris Hamilton, Kiyan Tavangar, the EXP collaboration, especially the Bars & Spirals working group, and the Gaia UB team for the valuable discussions that contributed to this paper. We acknowledge the grants PID2021-125451NA-I00 and CNS2022-135232 funded by MICIU/AEI/10.13039/501100011033 and by “ERDF A way of making Europe”, by the “European Union” and by the “European Union Next Generation EU/PRTR”, and the Institute of Cosmos Sciences University of Barcelona (ICCUB, Unidad de Excelencia ‘María de Maeztu’) through grant CEX2019-000918-M. MB acknowledges funding from the University of Barcelona’s official doctoral program for the development of a R+D+i project under the PREDOCS-UB grant. TA acknowledges the grant RYC2018-025968-I funded by MCIN/AEI/10.13039/501100011033 and by “ESF Investing in your future”. This research in part used computational resources of Pegasus provided by Multidisciplinary Cooperative Research Program in Center for Computational Sciences, University of Tsukuba.

References

- Aguilar, L. A. & White, S. D. M. 1985, *ApJ*, 295, 374
- Alves, E. P. & Fiuza, F. 2022, *Physical Review Research*, 4, 033192
- Anders, F., Khalatyan, A., Queiroz, A. B. A., et al. 2022, *A&A*, 658, A91
- Antoja, T., Helmi, A., Romero-Gómez, M., et al. 2018, *Nature*, 561, 360
- Antoja, T., Ramos, P., García-Conde, B., et al. 2023, *A&A*, 673, A115
- Antoja, T., Ramos, P., López-Guitart, F., et al. 2022, *A&A*, 668, A61
- Arora, A., Garavito-Camargo, N., Sanderson, R. E., et al. 2025, *arXiv e-prints*, arXiv:2504.20133
- Arora, A., Sanderson, R., Regan, C., et al. 2024, *ApJ*, 977, 23
- Asano, T., Fujii, M. S., Baba, J., Portegies Zwart, S., & Bédorf, J. 2025, *arXiv e-prints*, arXiv:2501.12436
- Beetham, S. & Capecelatro, J. 2020, *Physical Review Fluids*, 5, 084611
- Beetham, S., Fox, R. O., & Capecelatro, J. 2021, *Journal of Fluid Mechanics*, 914
- Bernet, M., Ramos, P., Antoja, T., et al. 2025, *A&A*, 697, A214
- Bernet, M., Ramos, P., Antoja, T., et al. 2022, *A&A*, 667, A116
- Bernet, M., Ramos, P., Antoja, T., Monari, G., & Famaey, B. 2024, *A&A*, 686, A92
- Binney, J. & Schönrich, R. 2018, *MNRAS*, 481, 1501
- Binney, J. & Tremaine, S. 2008, *Galactic Dynamics: Second Edition*
- Bland-Hawthorn, J. & Tepper-García, T. 2021, *MNRAS*, 504, 3168
- Bongard, J. & Lipson, H. 2007, *Proceedings of the National Academy of Sciences*, 104, 9943
- Bovy, J. 2015, *ApJS*, 216, 29
- Brunton, S. L. & Kutz, J. N. 2023, *arXiv e-prints*, arXiv:2303.17078
- Brunton, S. L., Proctor, J. L., & Kutz, J. N. 2016, *Proceedings of the National Academy of Science*, 113, 3932
- Cao, C., Li, Z.-Y., Schönrich, R., & Antoja, T. 2024, *ApJ*, 975, 292
- Cappellari, M. 2016, *ARA&A*, 54, 597
- Chakrabarti, S. & Blitz, L. 2009, *MNRAS*, 399, L118
- Chiba, R., Friske, J. K. S., & Schönrich, R. 2021, *MNRAS*, 500, 4710
- Cranmer, M. 2023, *arXiv preprint arXiv:2305.01582*
- Darling, K. & Widrow, L. M. 2019, *MNRAS*, 490, 114
- Darragh-Ford, E., Hunt, J. A. S., Price-Whelan, A. M., & Johnston, K. V. 2023, *ApJ*, 955, 74
- Dehnen, W. 1993, *MNRAS*, 265, 250
- den Brok, M., Carollo, C. M., Erroz-Ferrer, S., et al. 2020, *MNRAS*, 491, 4089
- Dobbs, C. & Baba, J. 2014, *PASA*, 31, e035
- Drimmel, R. & Spergel, D. N. 2001, *ApJ*, 556, 181
- Eilers, A.-C., Hogg, D. W., Rix, H.-W., et al. 2020, *ApJ*, 900, 186
- Erroz-Ferrer, S., Knapen, J. H., Leaman, R., et al. 2015, *MNRAS*, 451, 1004
- Fragkoudi, F., Katz, D., Trick, W., et al. 2019, *MNRAS*, 488, 3324
- Frankel, N., Bovy, J., Tremaine, S., & Hogg, D. W. 2023, *MNRAS*, 521, 5917
- Friske, J. K. S. & Schönrich, R. 2019, *MNRAS*, 490, 5414
- Fujii, M. S., Bédorf, J., Baba, J., & Portegies Zwart, S. 2019, *MNRAS*, 482, 1983
- Gaia Collaboration, Katz, D., Antoja, T., et al. 2018, *A&A*, 616, A11
- Gaia Collaboration, Prusti, T., de Bruijne, J. H. J., et al. 2016, *A&A*, 595, A1
- Georgelin, Y. M. & Georgelin, Y. P. 1976, *A&A*, 49, 57
- Ghosh, S., Saha, K., Jog, C. J., Combes, F., & Di Matteo, P. 2022, *MNRAS*, 511, 5878
- Goldreich, P. & Lynden-Bell, D. 1965, *MNRAS*, 130, 125
- Green, G. M., Ting, Y.-S., & Kamdar, H. 2023, *ApJ*, 942, 26
- Hernquist, L. 1990, *ApJ*, 356, 359
- Horta, D., Price-Whelan, A. M., Hogg, D. W., et al. 2024, *ApJ*, 962, 165
- Hunt, J. A. S., Bub, M. W., Bovy, J., et al. 2019, *MNRAS*, 490, 1026
- Hunt, J. A. S., Price-Whelan, A. M., Johnston, K. V., et al. 2024, *MNRAS*, 527, 11393
- Hunt, J. A. S., Stelea, I. A., Johnston, K. V., et al. 2021, *MNRAS*, 508, 1459
- Ibata, R. A., Gilmore, G., & Irwin, M. J. 1994, *Nature*, 370, 194
- Jiménez-Arranz, Ó., Chemin, L., Romero-Gómez, M., et al. 2024, *A&A*, 683, A102
- Jiménez-Arranz, Ó., Horta, D., van der Marel, R. P., et al. 2025, *A&A*, 698, A88
- Jiménez-Arranz, Ó., Romero-Gómez, M., Luri, X., et al. 2023, *A&A*, 669, A91
- Johnson, A. C., Petersen, M. S., Johnston, K. V., & Weinberg, M. D. 2023, *MNRAS*, 521, 1757
- Julian, W. H. & Toomre, A. 1966, *ApJ*, 146, 810
- Kalda, T., Green, G. M., & Ghosh, S. 2024, *MNRAS*, 527, 12284
- Kalnajs, A. J. 1971, *ApJ*, 166, 275
- Kalnajs, A. J. 1973, *PASA*, 2, 174
- Kawata, D., Baba, J., Ciucă, I., et al. 2018, *MNRAS*, 479, L108
- Kepler, J. 1609, *Astronomia nova ... seu physica coelestis, tradita commentariis de motibus stellae martis*
- Khalil, Y. R., Famaey, B., Monari, G., et al. 2024, *arXiv e-prints*, arXiv:2411.12800
- Laporte, C. F. P., Johnston, K. V., Gómez, F. A., Garavito-Camargo, N., & Besla, G. 2018, *MNRAS*, 481, 286
- Laporte, C. F. P., Minchev, I., Johnston, K. V., & Gómez, F. A. 2019, *MNRAS*, 485, 3134
- Lin, C. C. & Shu, F. H. 1964, *ApJ*, 140, 646
- Lynden-Bell, D. & Kalnajs, A. J. 1972, *MNRAS*, 157, 1
- Miyamoto, M. & Nagai, R. 1975, *PASJ*, 27, 533
- Navarro, J. F., Frenk, C. S., & White, S. D. M. 1996, *ApJ*, 462, 563
- North, J. S., Wikle, C. K., & Schliep, E. M. 2023, *International Statistical Review*, 91, 464
- Oeur, M., Loebman, S. R., Price-Whelan, A. M., et al. 2025, *arXiv e-prints*, arXiv:2505.05590
- Oh, S. H., Kim, W.-T., & Lee, H. M. 2015, *ApJ*, 807, 73
- Oh, S. H., Kim, W.-T., Lee, H. M., & Kim, J. 2008, *ApJ*, 683, 94
- Petersen, M. S., Roule, M., Fouvry, J.-B., Pichon, C., & Tep, K. 2024, *MNRAS*, 530, 4378
- Pettitt, A. R. & Wadsley, J. W. 2018, *MNRAS*, 474, 5645
- Price-Whelan, A. M. 2017, *The Journal of Open Source Software*, 2, 388
- Price-Whelan, A. M., Hogg, D. W., Johnston, K. V., et al. 2021, *ApJ*, 910, 17
- Price-Whelan, A. M., Hunt, J. A. S., Horta, D., et al. 2025, *ApJ*, 979, 115
- Ramos, P., Antoja, T., & Figueras, F. 2018, *A&A*, 619, A72
- Reid, M. J., Menten, K. M., Zheng, X. W., et al. 2009, *ApJ*, 700, 137
- Reinbold, P. A. K., Gurevich, D. R., & Grigoriev, R. O. 2020, *Phys. Rev. E*, 101, 010203
- Rozier, S., Famaey, B., Siebert, A., et al. 2022, *ApJ*, 933, 113
- Rozier, S., Fouvry, J. B., Breen, P. G., et al. 2019, *MNRAS*, 487, 711
- Rudy, S. H., Brunton, S. L., Proctor, J. L., & Kutz, J. N. 2017, *Science Advances*, 3, e1602614
- Sanders, R. H. & Huntley, J. M. 1976, *ApJ*, 209, 53
- Schaeffer, H. 2017, *Proceedings of the Royal Society of London Series A*, 473, 20160446
- Schaeffer, H. & McCalla, S. G. 2017, *Phys. Rev. E*, 96, 023302
- Schmelzer, M., Dwight, R. P., & Cinnella, P. 2020, *Flow, Turbulence and Combustion*, 104, 579
- Schmid, P. J. 2010, *Journal of Fluid Mechanics*, 656, 5
- Schmidt, M. & Lipson, H. 2009, *Science*, 324, 81
- Sellwood, J. A. & Carlberg, R. G. 1984, *ApJ*, 282, 61
- Sellwood, J. A. & Masters, K. L. 2022, *ARA&A*, 60 [arXiv:2110.05615]
- Struck, C., Dobbs, C. L., & Hwang, J.-S. 2011, *MNRAS*, 414, 2498
- Supekar, R., Song, B., Hastewell, A., et al. 2023, *Proceedings of the National Academy of Sciences*, 120, e2206994120
- Tenachi, W., Ibata, R., & Diakogiannis, F. I. 2023, *ApJ*, 959, 99
- Tenachi, W., Ibata, R., François, T. L., & Diakogiannis, F. I. 2024, *ApJ*, 969, L26
- Toomre, A. 1964, *ApJ*, 139, 1217
- Vasiliev, E. 2019, *MNRAS*, 482, 1525
- Vasiliev, E., Belokurov, V., & Erkal, D. 2021, *MNRAS*, 501, 2279
- Virtanen, P., Gommers, R., Oliphant, T. E., et al. 2020, *Nature Methods*, 17, 261
- Zachmanoglou, E. C. & Thoe, D. W. 1986, *Introduction to partial differential equations with applications* (Courier Corporation)
- Zanna, L. & Bolton, T. 2020, *Geophysical Research Letters*, 47, e2020GL088376
- Zucker, C., Saydjari, A. K., Speagle, J. S., et al. 2025, *arXiv e-prints*, arXiv:2503.02657

Appendix A: Radial profiles of the small impact

This appendix presents supplementary details and visualizations of the velocity structure resulting from the small, distant $m = 2$ kinematic kick simulation discussed in Section 2.1. Fig. A.1 shows the 1D radial profiles of the velocity perturbations ΔV_R (top row) and ΔV_ϕ (bottom row) as a function of radius R , specifically along the line $\phi = 0^\circ$, at five different times ($t = 0, 0.1, 0.2, 0.3, 0.4$ Gyr). Each panel breaks down the total velocity perturbation (black line) into the contributions from the two fundamental wave modes excited by the $m = 2$ kick: the $\Omega - \kappa/2$ mode (blue line) and the $\Omega + \kappa/2$ mode (purple line). These profiles visually demonstrate how the initial kick at $t = 0$ Gyr is composed of these two modes and how the spatial structure evolves over time. Notably, the $\Omega - \kappa/2$ mode contributes significantly to the overall perturbation pattern, while the $\Omega + \kappa/2$ mode is typically seen as smaller-scale radial variations superimposed on the dominant mode.

Appendix B: Analytical derivations

Appendix B.1: Derivation of the linear equations

We start by considering the Collisionless Boltzmann Equation in 2D Cylindrical Coordinates, for an axisymmetric potential without self-gravity:

$$\frac{\partial f}{\partial t} + v_R \frac{\partial f}{\partial R} + \left(\frac{v_\phi^2}{R} - \frac{\partial \Phi}{\partial R} \right) \frac{\partial f}{\partial v_R} - \frac{v_R v_\phi}{R} \frac{\partial f}{\partial v_\phi} = 0 \quad (\text{B.1})$$

Taking moments by multiplying by v_R and v_ϕ and integrating over the velocities yields the Jeans Equation for the mean velocities V_R and V_ϕ . We assume there is no velocity dispersion, so all stress-tensor terms drop out, matching the zero-dispersion setup of our simulations (Sect. 2). This yields:

$$\begin{aligned} \frac{\partial V_R}{\partial t} + V_R \frac{\partial V_R}{\partial R} + \frac{V_\phi}{R} \frac{\partial V_R}{\partial \phi} - \frac{V_\phi^2}{R} + \frac{\partial \Phi}{\partial R} &= 0, \\ \frac{\partial V_\phi}{\partial t} + V_R \frac{\partial V_\phi}{\partial R} + \frac{V_\phi}{R} \frac{\partial V_\phi}{\partial \phi} + \frac{V_R V_\phi}{R} &= 0. \end{aligned} \quad (\text{B.2})$$

We linearize the equation by assuming a small perturbation about the equilibrium of the form $V_\phi = V_c(R) + \Delta V_\phi$, $V_R = \Delta V_R$:

$$\begin{aligned} \frac{\partial \Delta V_R}{\partial t} + \Omega \frac{\partial \Delta V_R}{\partial \phi} - 2\Omega \Delta V_\phi &= 0, \\ \frac{\partial \Delta V_\phi}{\partial t} + \Omega \frac{\partial \Delta V_\phi}{\partial \phi} + \left(R \frac{d\Omega}{dR} + 2\Omega \right) \Delta V_R &= 0, \end{aligned} \quad (\text{B.3})$$

where $\Omega \equiv V_c/R = \sqrt{-\frac{1}{R} \frac{d\Phi}{dR}}$. Assuming $\kappa^2 = R \frac{d\Omega^2}{dR} + 4\Omega^2$ and $\gamma = \frac{2\Omega}{\kappa}$, we can rewrite the linearized equations to obtain the following system of equations:

$$\begin{aligned} \frac{\partial \Delta V_R}{\partial t} &= -\Omega \frac{\partial \Delta V_R}{\partial \phi} + \kappa \gamma \Delta V_\phi, \\ \frac{\partial \Delta V_\phi}{\partial t} &= -\Omega \frac{\partial \Delta V_\phi}{\partial \phi} - \frac{\kappa}{\gamma} \Delta V_R. \end{aligned} \quad (\text{B.4})$$

In the following section, we derive the analytical solution of the linear PDE recovered here (Eq. B.4).

Appendix B.2: Solution of the linear equations

For a fixed radius R , where $\Omega(R)$, $\kappa(R)$, and $\gamma(R)$ are constants, the linearized system (Eq. B.4) becomes a pair of linear PDEs with constant coefficients. Exponential functions like $e^{i(m\phi - \omega t)}$ are eigenfunctions of linear differential operators, simplifying the PDEs to algebraic equations. Therefore, we can assume solutions of the form

$$\Delta V_R = \Delta V_R^{m, \omega} e^{i(m\phi - \omega t)}, \quad \Delta V_\phi = \Delta V_\phi^{m, \omega} e^{i(m\phi - \omega t)}, \quad (\text{B.5})$$

where m is the azimuthal mode and ω is their frequency. Substituting these solutions in the linearized system and operating it, we obtain

$$\begin{aligned} (\omega - m\Omega) \Delta V_\phi^{m, \omega} &= \frac{\kappa}{i\gamma} \Delta V_R^{m, \omega}, \\ (\omega - m\Omega) \Delta V_R^{m, \omega} &= -\frac{\kappa\gamma}{i} \Delta V_\phi^{m, \omega}, \end{aligned} \quad (\text{B.6})$$

whose solution leads to the relation

$$\omega = m\Omega \pm \kappa, \quad (\text{B.7})$$

which tell us which eigenfunctions “survive”, i.e. which waves develop after the initial perturbation. The pattern speed of these waves ($\Omega_p \equiv \omega/m$) is then

$$\Omega_p = \Omega \pm \frac{\kappa}{m}. \quad (\text{B.8})$$

Finally, solving Eq. B.6 also gives the amplitude relation

$$\Delta V_\phi^{m, \omega} = \mp \frac{i}{\gamma} \Delta V_R^{m, \omega}, \quad (\text{B.9})$$

where the inverted \mp sign means that it is the opposite sign as the one obtained for $\Omega \pm \kappa/m$. Therefore, the analytical solution of the system consists of a sum of spiral density waves with frequencies $\omega = m\Omega \pm \kappa$:

$$\begin{aligned} \Delta V_R(R, \phi, t) &= \sum_m \left[a_m e^{i(m\phi - (m\Omega + \kappa)t)} + b_m e^{i(m\phi - (m\Omega - \kappa)t)} \right], \\ \Delta V_\phi(R, \phi, t) &= \sum_m \left[c_m e^{i(m\phi - (m\Omega + \kappa)t)} + d_m e^{i(m\phi - (m\Omega - \kappa)t)} \right], \end{aligned} \quad (\text{B.10})$$

where a_m, b_m, c_m, d_m are amplitudes determined by the initial conditions, and $c_m = -\frac{i}{\gamma} a_m$, $d_m = \frac{i}{\gamma} b_m$.

Appendix B.3: Small $m = 2$ impact

The initial velocity kick by the perturber from Equation 2 with a simple $m = 2$ mode with small amplitude can be written in compact, complex notation, as the real parts of

$$\Delta V_R = \epsilon R e^{i2\phi}, \quad \Delta V_\phi = i\epsilon R e^{i2\phi}. \quad (\text{B.11})$$

For an $m = 2$ mode, using the general solution (Eq. B.10) obtained in the previous section, we write

$$\begin{aligned} \Delta V_R &= a_2 e^{i(2\phi - (2\Omega + \kappa)t)} + b_2 e^{i(2\phi - (2\Omega - \kappa)t)}, \\ \Delta V_\phi &= c_2 e^{i(2\phi - (2\Omega + \kappa)t)} + d_2 e^{i(2\phi - (2\Omega - \kappa)t)}. \end{aligned} \quad (\text{B.12})$$

At $t = 0$, the solution must match the initial conditions, that is:

$$\Delta V_R(0) = (a_2 + b_2) e^{i2\phi} = \epsilon R e^{i2\phi}, \quad (\text{B.13})$$

$$\Delta V_\phi(0) = (c_2 + d_2) e^{i2\phi} = \frac{i}{\gamma} (-a_2 + b_2) e^{i2\phi} = i\epsilon R e^{i2\phi}, \quad (\text{B.14})$$

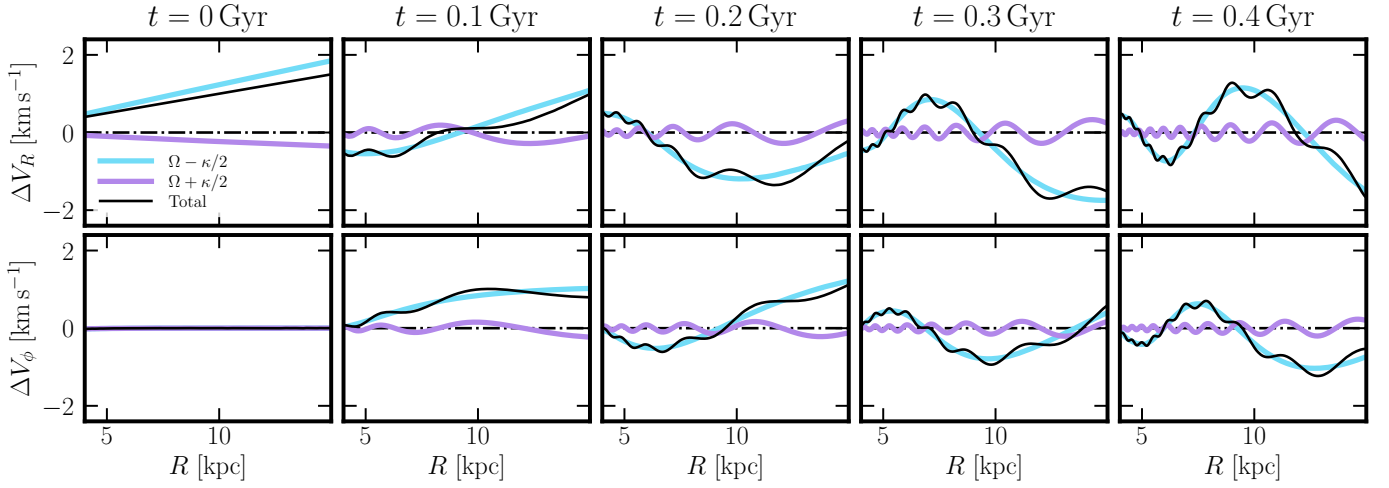


Fig. A.1. Radial profiles of velocity perturbations ΔV_R (top row) and ΔV_ϕ (bottom row) for the small, distant, $m = 2$ kinematic kick simulation (Sect. 2.1), as a function of R , at four different times, at $\phi = 0^\circ$. In each panel, the blue line represents the contribution from the $\Omega - \kappa/2$ wave, the purple line represents the $\Omega + \kappa/2$ wave, and the black line is the sum of these two modes, which corresponds to the total velocity perturbation at that radius. The initial kick ($t = 0$ Gyr) decomposes into the two modes. As time evolves, the $\Omega - \kappa/2$ mode remains dominant and shapes the overall perturbation pattern, while the $\Omega + \kappa/2$ mode appears as smaller-scale radial oscillations on top of it.

where we used the eigenmode relation $c_2 = -\frac{i}{\gamma}a_2$, $d_2 = \frac{i}{\gamma}b_2$. This immediately gives

$$\begin{aligned} a_2 + b_2 &= \epsilon R, \\ -a_2 + b_2 &= \gamma \epsilon R. \end{aligned} \quad (\text{B.15})$$

Solving these two simple equations for a_2 and b_2 , we obtain the amplitude of the surviving modes

$$a_2 = \epsilon R \frac{1 - \gamma}{2}, \quad b_2 = \epsilon R \frac{1 + \gamma}{2}. \quad (\text{B.16})$$

Substituting these amplitudes, along with the corresponding $c_2 = -\frac{i}{\gamma}a_2$ and $d_2 = \frac{i}{\gamma}b_2$, back into the general solution form (Eq. B.12) shows the time evolution of the perturbation:

$$\begin{aligned} \Delta V_R &= \epsilon R \frac{1 - \gamma}{2} e^{i(2\phi - (2\Omega + \kappa)t)} + \epsilon R \frac{1 + \gamma}{2} e^{i(2\phi - (2\Omega - \kappa)t)}, \\ \Delta V_\phi &= -\frac{i}{\gamma} \epsilon R \frac{1 - \gamma}{2} e^{i(2\phi - (2\Omega + \kappa)t)} + \frac{i}{\gamma} \epsilon R \frac{1 + \gamma}{2} e^{i(2\phi - (2\Omega - \kappa)t)}. \end{aligned} \quad (\text{B.17})$$

These expressions clearly show that the initial impulsive condition at $t = 0$ has decomposed into a superposition of two distinct waves, with amplitudes a_2 and b_2 . Thus, the relative amplitude of these waves is directly determined by

$$\frac{\mathcal{A}_{\Omega - \kappa/2}}{\mathcal{A}_{\Omega + \kappa/2}} = \frac{|b_2|}{|a_2|} = \frac{1 + \gamma}{\gamma - 1} \quad (\text{B.18})$$

where we used that $\gamma > 1$ to remove the absolute values.

Appendix C: Basis Function evolution

The linear PDE system (Eq. B.4) obtained in Sect. 4 (Appendix B.1) governs the evolution of the small impact system. We can solve this PDE system efficiently by expressing the velocity perturbations in terms of coefficients from a basis function expansion. Using this method, the linear PDE system is transformed into a system of coupled ODEs for the time-dependent coefficients, allowing us to evolve the system “only” in the coefficient space.

We expand the perturbations $\Delta V_R(R, \phi)$ and $\Delta V_\phi(R, \phi)$ in an orthonormal basis function. For the angular direction, we use the full complex Fourier basis, while in the radial direction we adopt a general orthonormal basis $\{G_n(r)\}$ defined on the interval $R_{\min} \leq r \leq R_{\max}$. That is, we write

$$\Delta V_R(R, \phi) = \sum_{m,n} \alpha_{m,n} u_m(\phi) G_n(r) \quad (\text{C.1})$$

$$\Delta V_\phi(R, \phi) = \sum_{m,n} \beta_{m,n} u_m(\phi) G_n(r),$$

where the angular and radial basis functions are given by

$$u_m(\phi) = \frac{1}{\sqrt{2\pi}} e^{im\phi}, \quad (\text{C.2})$$

and the radial basis functions satisfy the orthonormality condition

$$\int_{R_{\min}}^{R_{\max}} r dr G_n(r) G_{n'}(r) = \delta_{n,n'}. \quad (\text{C.3})$$

Assuming that the quantities $\Delta V_R, \Delta V_\phi$ evolve in time according to Eq. B.4, we substitute them by our basis functions equations (Eq. C.1). Below we show an example of how we proceed with the $\Omega \frac{\partial \Delta V_R}{\partial \phi}$ term. Since it is a linear system, the calculation is equivalent for all the other terms of the system.

After inserting the basis expansion, the $\Omega \frac{\partial \Delta V_R}{\partial \phi}$ term takes the form

$$\Omega(r) \sum_{m,n} i m \alpha_{m,n}(t) u_m(\phi) G_n(r) \quad (\text{C.4})$$

where we have used that $\frac{\partial}{\partial \phi} u_m(\phi) = i m u_m(\phi)$. To isolate the evolution of a particular coefficient $\alpha_{m,n}(t)$, we project this expression onto the basis by multiplying it by $u_m^*(\phi) G_n(r)$ and integrating over the entire domain

$$\int_0^{2\pi} d\phi \int r dr u_m^*(\phi) G_n(r) \left[\sum_{m',n'} \alpha_{m',n'}(t) u_{m'}(\phi) \Omega(r) G_{n'}(r) \right].$$

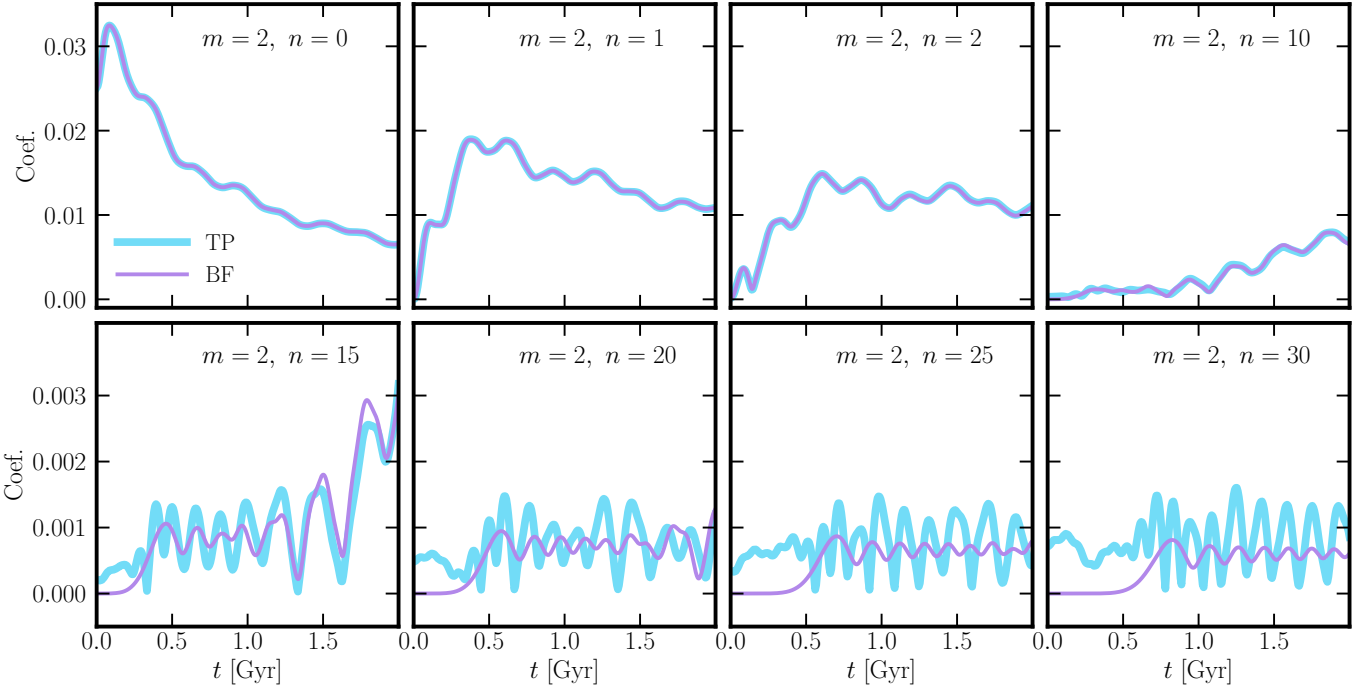


Fig. C.1. Temporal series of the basis function coefficients after a small $m = 2$ impact (Sect. 2). In blue, we show the basis function coefficient at each snapshot of the test particle simulation. In purple, we initialize the coefficients $\alpha_{m,n}(t = 0)$ and $\beta_{m,n}(t = 0)$ analytically and evolve them using Eq. C.10.

Due to the orthonormality of the angular basis functions $u_m(\phi)$, the expression simplifies to

$$\sum_{n'} \alpha_{m,n'}(t) \Omega_{n,n'}, \quad (\text{C.5})$$

where the radial coupling integral is defined by

$$\Omega_{n,n'} = \int r dr G_n(r) \Omega(r) G_{n'}(r). \quad (\text{C.6})$$

One can proceed identically with the rest of the terms in Eq. B.4. Only the terms with $\partial/\partial\phi$ have the im factor. The derivation for the left part of the system, the temporal derivatives, leads to a coupling integral

$$I_{n,n'} = \int r dr G_n(r) G_{n'}(r). \quad (\text{C.7})$$

where the identity matrix appears due to the orthonormality of the radial basis.

After the projection of the entire system, the time evolution of the expansion coefficients corresponding to a given angular mode m can be written as a system of coupled ODEs:

$$\begin{aligned} \dot{\alpha}_{m,n} &= -im \sum_{n'} \Omega_{n,n'} \alpha_{m,n'} + \sum_{n'} (\kappa\gamma)_{n,n'} \beta_{m,n'}, \\ \dot{\beta}_{m,n} &= -im \sum_{n'} \Omega_{n,n'} \beta_{m,n'} - \sum_{n'} \left(\frac{\kappa}{\gamma}\right)_{n,n'} \alpha_{m,n'}, \end{aligned} \quad (\text{C.8})$$

where $(\kappa\gamma)_{n,n'}$ and $(\kappa/\gamma)_{n,n'}$ are constructed using an analogue to Eq. C.7. In compact block-matrix notation for each m , this system is expressed as

$$\frac{d}{dt} \begin{pmatrix} \alpha_{m,n} \\ \beta_{m,n} \end{pmatrix} = \begin{pmatrix} -im\Omega_{n,n'} & (\kappa\gamma)_{n,n'} \\ (\frac{\kappa}{\gamma})_{n,n'} & -im\Omega_{n,n'} \end{pmatrix} \begin{pmatrix} \alpha_{m,n} \\ \beta_{m,n} \end{pmatrix}, \quad (\text{C.9})$$

and can be solved numerically (e.g. using matrix exponentiation). This conversion of PDEs into ODEs using basis function expansion (BFE) is a core technique in galactic dynamics, often used in spectral methods and the response-matrix framework (e.g. Kalnajs 1971; Rozier et al. 2019, 2022; Petersen et al. 2024). It transforms the differential operators in the PDE into algebraic operations on the time-dependent basis coefficients, allowing for efficient time evolution directly in coefficient space.

In Fig. C.1 we show the evolution of different n coefficients of the orthogonal basis function for the test particle simulation (TP, blue lines). For this run, we used a Legendre polynomial basis in the radial direction. Using the analytical impact formula, we compute the initial $\alpha_{m,n}, \beta_{m,n}$ coefficients, and evolve them using Eq. C.10 (BF, purple lines). We observe a great match between both methods in the low order coefficients. In the high order coefficients, we notice that we can go well below the noise threshold, and still capture a significant signal. This demonstrates the accuracy and efficiency of evolving the system in coefficient space for the linear case.

Applying this spectral approach to the SINDy-discovered non-linear PDE for the large-impact scenario (Eq. 10) is more challenging than the linear case because non-linear terms introduce complex couplings between the basis coefficients. However, solving the resulting system of ODEs for the coefficients would still be significantly faster than running full particle simulations or solving the non-linear PDE numerically. This method could be applied to more complex SINDy-discovered PDEs, perhaps including self-gravity terms, offering an efficient way to explore the parameter space of galactic perturbations.

Appendix D: Realistic Simulation Details

This appendix provides detailed information about the realistic simulations used in Section 5.

***N*-body simulation** We use the *N*-body simulation of a Sgr-like impact, presented in Asano et al. (2025), which is an extension of the original models described in Fujii et al. (2019). In this model, the MW-like host galaxy is constructed with a three-component structure: a DM halo, a classical bulge, and an exponential stellar disc. The DM halo follows an NFW profile (Navarro et al. 1996) with a scale radius of 10 kpc and a mass of $M_h = 8.68 \times 10^{11} M_\odot$. The bulge is modelled with a Hernquist (1990) profile having a scale radius of 0.75 kpc and a mass of $5.42 \times 10^9 M_\odot$. The stellar disc is characterized by an exponential radial profile with a scale radius of 2.3 kpc, a vertical scale height of 0.2 kpc, and a total mass of $3.61 \times 10^{10} M_\odot$. The stellar disc contains 213M particles. The Sgr-like satellite has a DM component that follows an NFW profile with a total mass of $5 \times 10^{10} M_\odot$ and a scale radius of 7.5 kpc, while its stellar component is represented by a Hernquist profile with a mass of $1 \times 10^9 M_\odot$ and a scale radius of 2 kpc.

From this simulation, we select the time range starting 250 Myr after the first pericentre ($t = 0.9$ Gyr) for our analysis. This period resembles the tidal spiral phase before the appearance of kinematic crossings (Eq. 20) becomes significant.

Test Particle Rerun TPR Complementing this *N*-body simulation, Asano et al. (2025, in prep.) have run a suite of test particle reruns of the previous *N*-body model using Agama. Here we used one of them, which we call TPR, to isolate and test the contribution of self-gravity to the SINDy analysis compared to a frozen potential. In this run, the initial conditions (ICs) of the disc particles are those of the *N*-body at the first pericentre time ($t = 0.9$ Gyr). The particles are then evolved in the isolated frozen axisymmetric potential of the MW host galaxy, effectively removing the self-gravity of the disc and halo, as well as the external acceleration from the perturber. The evolution of this simplified model is shown alongside the *N*-body maps in the second and fourth columns of Fig. 7.